

2020

## Battery-Free Antenna Sensors for Strain and Crack Monitoring: Technical Report

Yang Wang

Georgia Institute of Technology, [yang.wang@ce.gatech.edu](mailto:yang.wang@ce.gatech.edu)

Dan Lin

Follow this and additional works at: [https://scholarsmine.mst.edu/project\\_sn-2](https://scholarsmine.mst.edu/project_sn-2)



Part of the [Structural Engineering Commons](#)

---

### Recommended Citation

Wang, Yang and Lin, Dan, "Battery-Free Antenna Sensors for Strain and Crack Monitoring: Technical Report" (2020). *Project SN-2*. 2.

[https://scholarsmine.mst.edu/project\\_sn-2/2](https://scholarsmine.mst.edu/project_sn-2/2)

This Technical Report is brought to you for free and open access by Scholars' Mine. It has been accepted for inclusion in Project SN-2 by an authorized administrator of Scholars' Mine. This work is protected by U. S. Copyright Law. Unauthorized use including reproduction for redistribution requires the permission of the copyright holder. For more information, please contact [scholarsmine@mst.edu](mailto:scholarsmine@mst.edu).



# FINAL REPORT

#INSPIRE-001  
& CII-001

GRANT NO: 69A3551747126

GRANT PERIOD: 11/30/16 – 09/30/22

PROJECT PERIOD: 06/01/17 – 12/31/19

## Inspecting and Preserving Infrastructure through Robotic Exploration (INSPIRE)

Tier 1 University Transportation Center Sponsored by the Office of the Assistant Secretary for Research and Technology (OST-R)



<b>Project/Report Title:</b>	<b>Battery-Free Antenna Sensors for Strain and Crack Monitoring</b>
<b>Consortium Member:</b>	Georgia Institute of Technology
<b>Principal Investigator:</b>	Yang Wang, Ph.D.
<b>Co-Principal Investigator(s):</b>	
<b>Report Authors:</b>	Yang Wang, and Dan Li



The City College  
of New York



UNLV



LINCOLN

OZARKS TECHNICAL  
COMMUNITY COLLEGE





## DISCLAIMER

*The contents of this report reflect the views of the authors, who are responsible for the facts and the accuracy of the information presented herein. This document is disseminated in the interest of information exchange. The report is funded, partially or entirely, by a grant from the U.S. Department of Transportation's University Transportation Centers Program. However, the U.S. Government assumes no liability for the contents or use thereof.*



**TECHNICAL REPORT DOCUMENTATION PAGE**

<b>1. Report No.</b> INSPIRE-001 & CII-001	<b>2. Government Accession No.</b> (blank)	<b>3. Recipient's Catalog No.</b> (blank)	
<b>4. Title and Subtitle</b> Battery-Free Antenna Sensors for Strain and Crack Monitoring		<b>5. Report Date</b> 01/31/2020	
		<b>6. Performing Organization Code (blank)</b>	
<b>7. Author(s)</b> Yang Wang, and Dan Li		<b>8. Performing Organization Report No.</b> Project # (blank)	
<b>9. Performing Organization Name and Address</b> Georgia Institute of Technology 790 Atlantic Dr NW Atlanta, GA 30332-0355		<b>10. Work Unit No.</b> (blank)	
		<b>11. Contract or Grant No.</b> USDOT #69A3551747126	
<b>12. Sponsoring Agency Name and Address</b> Office of the Assistant Secretary for Research and Technology U.S. Department of Transportation 1200 New Jersey Avenue, SE Washington, DC 20590		<b>13. Type of Report and Period Covered</b> Final Report Period: 06/01/2017 – 12/31/2019	
		<b>14. Sponsoring Agency Code</b>	
<b>15. Supplementary Notes</b> The investigation was conducted under the auspices of the INSPIRE University Transportation Center.			
<b>16. Abstract</b> This project studies a wireless patch antenna as a novel strain/crack sensing technique for structural health monitoring (SHM). The strain/crack induced resonance frequency shift of the antenna can be wirelessly detected and utilized to estimate the surface strain and crack propagation. However, temperature fluctuation can generate some unwanted changes in resonance frequency and introduce significant noises in measurement. This project studies a thermally stable patch antenna sensor through both numerical simulations and laboratory experiments. Using a substrate material with a steady dielectric constant, a patch antenna sensor is designed to perform reliably under temperature fluctuations. In addition, a dual-mode patch antenna sensor is designed to achieve long interrogation distance. Various types of materials used in substrate are investigated through laboratory tests. Strain/crack sensing performance has been validated through multi-physics simulations and experiments. The patch antenna sensors are demonstrated to be effective in wireless strain/crack measurements and have potential for large-scale monitoring of structures.			
<b>17. Key Words</b> Patch antenna sensor, thermal stability, strain, crack, wireless sensing, RFID		<b>18. Distribution Statement</b> No restrictions. This document is available to the public.	
<b>19. Security Classification (of this report)</b> Unclassified	<b>20. Security Classification (of this page)</b> Unclassified	<b>21. No of Pages</b> 56	



## EXECUTIVE SUMMARY

In this project, a thermally stable Radiofrequency Identification (RFID) patch antenna sensor and a dual-mode RFID patch antenna sensor were designed for wireless strain/crack measurements. Deformation of a patch antenna causes its electromagnetic resonance frequency to shift. This resonance frequency shift can be wirelessly identified by reader interrogation and used to estimate surface strain/crack. Using the RFID technology, the response signal from a patch antenna sensor can be conveniently modulated and distinguished from environmental reflection. In addition, a dual-mode antenna sensor is designed for long-distance interrogation. With the assistance of a power management circuitry, the dual-mode sensor can work in both passive (battery-free) and active (battery-assisted) modes. When solar charging is available for a coin cell battery, the active mode requires less radiofrequency (RF) signal from the reader interrogation and thus achieves long interrogation distance. When the battery energy is depleted, the sensor automatically falls back into the passive mode.

Thermal stability of the sensors is validated through temperature chamber testing and outdoor field testing. The nonlinear constitutive relationships of the substrate material along two orthogonal directions are investigated through tensile testing. The dielectric constant change of the substrate material under strain is quantified through laboratory experiments. In addition, the strain transfer ratio of the antenna sensor is studied by both the numerical simulations and tensile tests. The parameters of the nonlinear constitutive model of adhesive between the antenna sensor and base structure is updated based on the strain transfer ratio data. These material properties are incorporated into a multi-physics coupled simulation to improve the accuracy of modelling in both mechanical and electromagnetic behaviors of the antenna sensor. Tensile and emulated crack tests are conducted to validate the strain sensing and crack sensing performances of the designed antenna sensors.



## ACKNOWLEDGMENT

Financial support for this INSPIRE UTC project was provided by the U.S. Department of Transportation, Office of the Assistant Secretary for Research and Technology (USDOT/OST-R) under Grant No. 69A3551747126 through INSPIRE University Transportation Center (<http://inspire-utc.mst.edu>) at Missouri University of Science and Technology. The views, opinions, findings and conclusions reflected in this publication are solely those of the authors and do not represent the official policy or position of the USDOT/OST-R, or any State or other entity.

## Table of Contents

1	DESCRIPTION OF THE PROBLEM .....	7
2	APPROACH .....	10
2.1	Thermally stable RFID patch antenna sensor .....	10
2.2	Dual-mode RFID patch antenna sensor .....	12
3	METHODOLOGY .....	13
3.1	Material testing and model updating .....	13
3.1.1	Thermal tests .....	13
3.1.1.1	Chamber test.....	13
3.1.1.2	Outdoor test.....	17
3.1.2	Mechanical parameter updating.....	18
3.1.2.1	Tensile test for substrate .....	18
3.1.2.2	Strain transfer ratio.....	26
3.1.3	Electromagnetic parameter updating.....	30
3.2	Multi-physics simulation .....	34
3.3	Strain sensing test.....	36
3.3.1	Compressive test.....	36
3.3.2	Tensile test .....	38
3.3.2.1	RFID patch antenna sensor .....	38
3.3.2.2	Dual-mode RFID patch antenna sensor .....	40
3.4	Crack sensing test .....	43
3.4.1	Emulated crack test.....	43
3.4.2	Fatigue crack test .....	45
4	FINDINGS.....	49
4.1	Thermal stability .....	49
4.2	Material property testing.....	49
4.3	Multi-physics simulation .....	50
4.4	Strain sensing performance .....	51
4.5	Crack sensing performance.....	51
5	CONCLUSION.....	53
6	RECOMMENDATIONS DEVELOPED AS A RESULT OF THE PROJECT .....	55
7	REFERENCES.....	56

## 1 DESCRIPTION OF THE PROBLEM

In order to accurately assess deterioration of civil, mechanical, and aerospace structures, intensive research in structural health monitoring (SHM) has been inspired over the past few decades. SHM systems can advance time-based maintenance into more effective condition-based maintenance. Sensors have been developed to measure various structural responses and operating conditions, including strain, displacement, acceleration, humidity, temperature, etc. Among the measurements, strain can be an important indicator for stress concentration and fatigue crack development. Metal foil strain gauges are currently among the most common solutions for strain measurement, owing to their low-cost, simple circuitry, and acceptable reliability in many applications. However, when applied to large structures, traditional metal foil strain gauges require lengthy cable connections for power supply and data acquisition, which can significantly increase installation time and system costs.

Among many new SHM technologies, wireless sensing can help to significantly reduce instrumentation time and system costs. A wireless sensing device usually has three functional modules: sensing interface (converting analog sensor signal to digital data), computing core (data storage and processing), and wireless transceiver (digital communication with peers or a wireless gateway server). To obtain different types of measurements, various sensors can be connected with the sensing interface of a wireless sensing device. For example, strain measurement is obtained by interfacing the device with a metal foil strain gauge. However, the requirement on batteries or other power sources limits the application scope of current wireless devices.

To address the challenge of power sources, passive wireless sensors have been proposed and investigated for SHM application. A passive wireless sensor can operate without onboard power supply. Among various types of passive sensors, passive wireless antenna sensors are known for their simplicity. Besides

achieving wireless communication, researchers have harnessed patch antennas to measure structural strain through the antenna resonance frequency change. Yi *et al* [1, 2] proposed passive (battery-free) RFID antennas for wireless strain measurement, using signal modulation by an economic RFID chip. Utilizing far-field effect, the RFID patch antenna sensors achieved longer interrogation distances and showed promising performance for wireless strain/crack sensing.

However, besides structural strain, other environmental disturbances, such as temperature fluctuation, can also result in the resonance frequency change of the antenna. A large frequency change due to temperature fluctuation can be difficult to distinguish from strain effects. To reduce temperature effect on resonance frequency, this work investigates the performance of thermally stable wireless antenna sensors.

A thermally stable substrate material RT/duroid® 6202 is chosen as the substrate for the antenna sensor. Mechanical and electromagnetic properties of the RT/duroid® 6202 are characterized through laboratory experiments and model updating technique. Using the updated material parameters, multi-physics simulation is performed to describe both mechanical and electromagnetic behaviors of the antenna sensor.

Despite the advantages of operating without onboard power supply, the passive patch antenna sensor supports limited interrogation distance. To increase the interrogation distance when battery power is available, a dual-mode patch antenna sensor is designed. The patch antenna sensor and a power management circuitry are fabricated on the same piece of substrate. When incorporated with a solar panel, the circuitry charges a coin cell battery and powers the RFID chip. With the help of solar charged battery power, the sensor requires less RF power for responding to reader interrogation, and thus achieves longer interrogation distance. On the other hand, when the battery power is depleted, the sensor





can still operate in passive mode relying on the RF power from the reader interrogation. This work has investigated the strain sensing performance of the dual-mode patch antenna sensor in both passive and active modes.

## 2 APPROACH

In order to reduce the noise caused by temperature fluctuation, patch antenna sensors are designed based on thermally stable dielectric substrate RT/duroid® 6202. In addition, a dual-mode patch antenna is designed to achieve long interrogation distance.

### 2.1 Thermally stable RFID patch antenna sensor

An RFID patch antenna sensor can be used to wirelessly measure the strain and/or crack on a structural surface through the shift of its electromagnetic resonance frequency. Fig. 2-1 illustrates the patch antenna sensor. The antenna sensor has copper cladding and RFID chip mounted on the top side of the dielectric substrate. Vias connect the top copper cladding to the ground plane. The RFID chip is used for wireless communication. The matching lines are designed to achieve the best impedance matching between the RFID chip and the antenna.

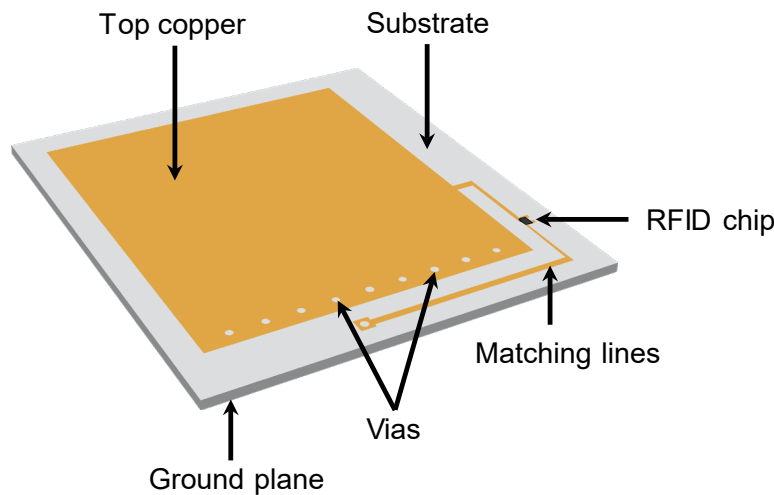


Fig. 2-1 RFID antenna as wireless antenna sensor for strain and crack sensing

According to electromagnetic theory, the resonance frequency  $f_R$  of a folded patch antenna can be calculated as:

$$f_R(\varepsilon, T) = \frac{c}{4L(1 + \varepsilon)\sqrt{\beta_r(T)}} \approx f_R(0, T)(1 - \varepsilon) \quad (2.1)$$

where  $\varepsilon$  is the strain applied on the antenna sensor;  $T$  is the environmental temperature;  $c$  is the speed of light;  $L$  is the length of the patch antenna;  $\beta_r$  is the effective dielectric constant of the substrate depending on temperature  $T$ .

As shown in Eq. (2.1), at a constant environmental temperature, the resonance frequency of a patch antenna sensor has an approximately linear relationship with strain  $\varepsilon$ , especially when the strain  $\varepsilon$  is small. This approximately linear relationship indicates that by measuring the antenna resonance frequency, the applied strain can be derived. Previous research has proposed the patch antenna sensor with RT/duroid® 5880 substrate, as shown in Fig. 2-2(a). Both numerical simulation and experimental testing have validated the strain sensing and crack sensing performance of the patch antenna sensor. According to Eq. (2.1), besides structural strain, temperature fluctuation can also result in the resonance frequency change of the antenna. Further research has proven that under temperature fluctuation, the design with RT/duroid® 5880 substrate undergoes large resonance frequency change due to its large dielectric constant variation [3]. To improve sensor reliability when temperature fluctuates, a thermally stable substrate material RT/duroid® 6202 is chosen to improve the sensor performance. In addition, a new RFID chip (NXP SL3S1013) with much smaller footprint (1.00×1.45 mm<sup>2</sup>) is adopted. A new version of passive patch antenna sensor is designed according to the dielectric constant of the substrate and the impedance (21.2 - j 199.7 Ohm) of the RFID chip (Fig. 2-2(b)).

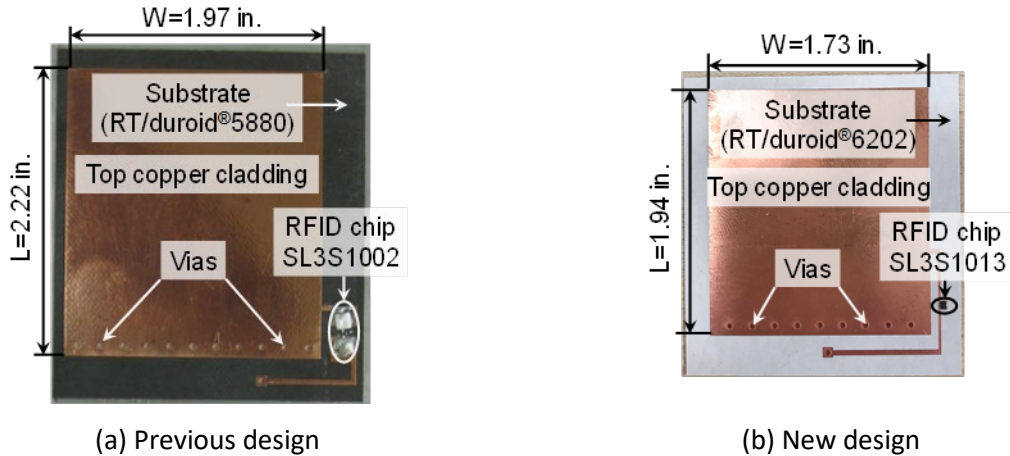


Fig. 2-2 Prototypes of passive patch antenna sensor

## 2.2 Dual-mode RFID patch antenna sensor

In order to increase the interrogation distance of a patch antenna sensor, a dual-mode RFID antenna sensor is designed. Equipped with a power management circuitry, this sensor is capable of harvesting solar energy, storing energy in a rechargeable coin battery, and operating in active mode. On the other hand, when the battery power is depleted, the sensor can still operate in passive mode and receive all operating energy wirelessly from the RFID reader. Fig. 2-3 shows design drawing and photo of the dual-mode patch antenna sensor.

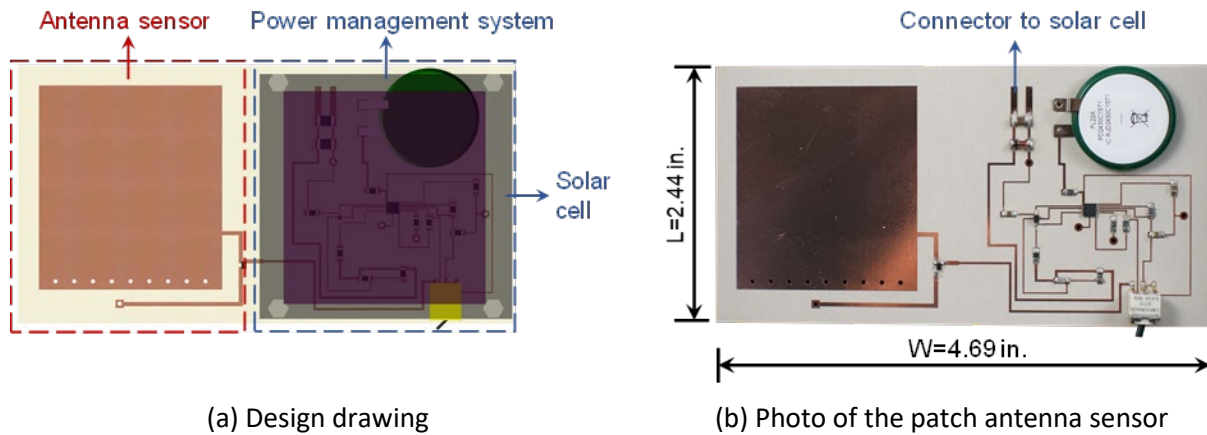


Fig. 2-3 Dual-mode RFID antenna sensor

### 3 METHODOLOGY

Numerical simulation and laboratory experiments are conducted to investigate the designed patch antenna sensors, in regard to thermal stability, mechanical and electromagnetic properties, strain sensing performance, and crack sensing performance.

#### 3.1 Material testing and model updating

Various material properties are presented in this section. Section 3.1.1 investigates the thermal stability of the substrate material RT/duroid® 6202. Section 3.1.2 describes the nonlinear constitutive relationships of the substrate material along two orthogonal directions and the strain transfer ratio of the antenna sensor. Section 3.1.3 presents the dielectric constant and strain relationship of the substrate.

##### 3.1.1 Thermal tests

A temperature chamber test and an outdoor test have been performed to study the thermal effect in the new antenna sensor.

###### 3.1.1.1 Chamber test

Temperature chamber test is conducted to study the antenna resonance frequency change caused by temperature fluctuation. Fig. 3-1 shows the temperature chamber test setup. An antenna sensor together with an aluminum specimen is placed in the chamber. Reader antenna is placed facing the sensor for wireless interrogation. Because all walls, ceiling, and floor of the temperature chamber are furnished with metal surfaces, a large amount of electromagnetic wave reflection to the reader interrogation signal is expected. To reduce the effect of reflection on wireless interrogation, four pieces of radiation-absorbent foams are placed around the test specimen and reader antenna. To keep track of temperature fluctuations in the chamber, a thermometer is placed around the foams, as shown in Fig. 3-1.



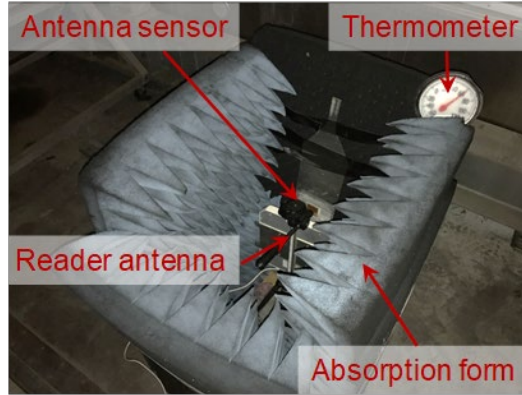


**Fig. 3-1 Experimental Setup**

Fig. 3-2 shows the temperature steps of the test. The chamber temperature is first increased to 123°F within 30 minutes and held at 123°F for 1 hour to achieve uniformity and stability. During the test, the chamber temperature is reduced to 37°F gradually. Interrogation power threshold measurement is conducted at each temperature level, before temperature reduction to the next level.

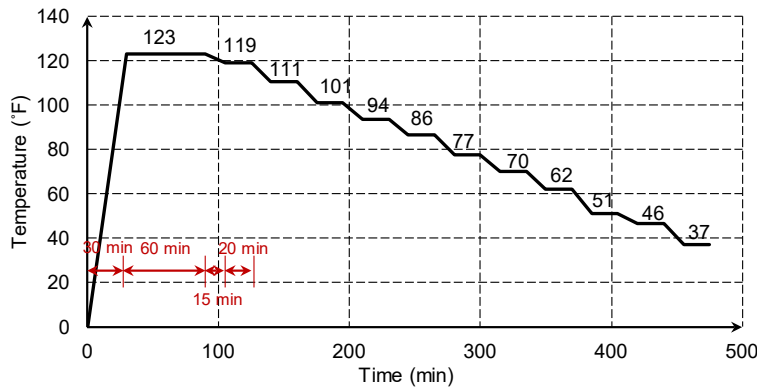
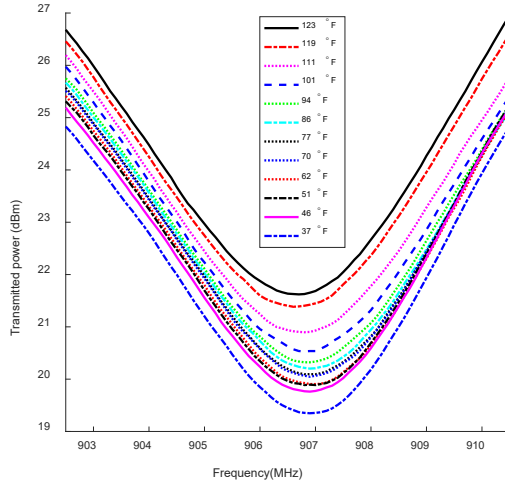


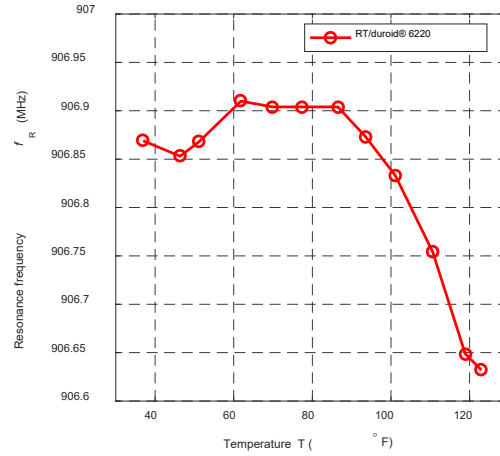
**Fig. 3-2 Target temperature levels during temperature chamber test**

To reduce environmental noise, five frequency sweeps are performed in the measurement at each temperature level. The average interrogation power threshold at different temperature levels are plotted in Fig. 3-3(a). Resonance frequency of the antenna sensor at each temperature level is extracted from the

interrogation power threshold curve. The resonance frequencies of the antenna sensor during the temperature fluctuation are plotted in Fig. 3-3(b). A total of about 0.3 MHz resonance frequency change is observed when the chamber temperature reduces from 123 °F to 37 °F.



(a) Average interrogation power



(b) Resonance frequency change during temperature fluctuation

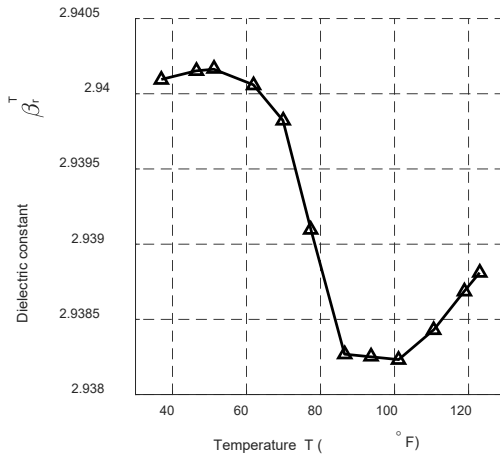
**Fig. 3-3 Temperature chamber test results (antenna sensor with RT/duroid® 6202 substrate)**

The resonance frequency change is caused by both thermal deformation and substrate dielectric constant change. Fig. 3-4(a) shows RT/duroid® 6202 dielectric constant change due to temperature fluctuation. Define the zero-strain resonance frequency  $f_{R0}$  at room temperature  $T_{ref} = 77$  °F as reference state of the sensor. The resonance frequency at another temperature  $T$  is calculated as:

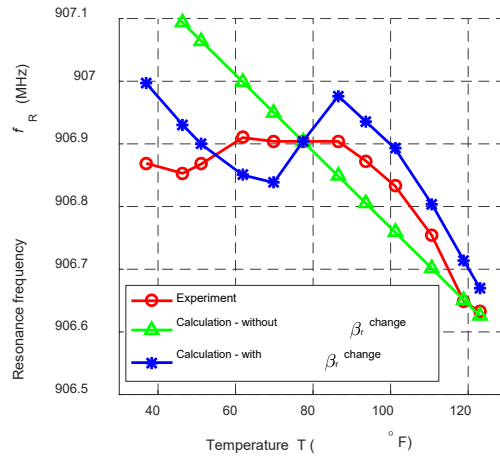
$$f_R(\epsilon, T) = f_R(\epsilon, T_{ref}) \sqrt{\frac{\beta_r(T_{ref})}{\beta_r(T)}} = (f_{R0} + \Delta f_R) \sqrt{\frac{\beta_r(T_{ref})}{\beta_r(T)}} \approx f_{R0} \sqrt{\frac{\beta_r(T_{ref})}{\beta_r(T)}} + S_T \cdot \Delta T \sqrt{\frac{\beta_r(T_{ref})}{\beta_r(T)}} \quad (3.1)$$

where  $\Delta T$  is the temperature difference from 77°F reference;  $\Delta f_R (\approx S_T \cdot \Delta T)$  is the resonance frequency change due to thermal expansion. Fig. 3-4(b) shows the comparison on resonance frequency change between the calculation and experimental data during temperature fluctuation. The comparison indicates

that without considering the substrate dielectric constant change with temperature fluctuation, the difference between calculation and experimental data is quite large. On the other hand, the calculation matches the experimental data closely when considering the substrate dielectric constant change with temperature fluctuation.



(a) Dielectric constant change during temperature fluctuation



(b) Resonance frequency change during temperature fluctuation

**Fig. 3-4 Effect of dielectric constant change during temperature fluctuation (RT/duroid® 6202 substrate)**

Previous research has shown that the patch antenna sensor with RT/duroid® 5880 substrate experienced approximately 5 MHz resonance frequency change when the temperature changed from 110 °F to 32 °F [3]. Fig. 3-5 shows the resonance frequency change of the antenna sensor with RT/duroid® 5880 substrate during the temperature fluctuation. The comparison between two different types of substrate materials clearly indicates that RT/duroid® 6202 substrate provides much better thermal stability.

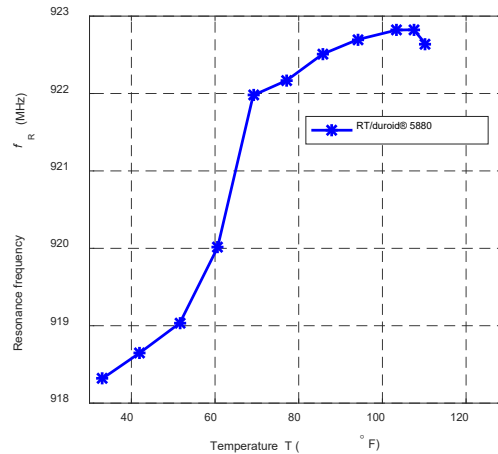


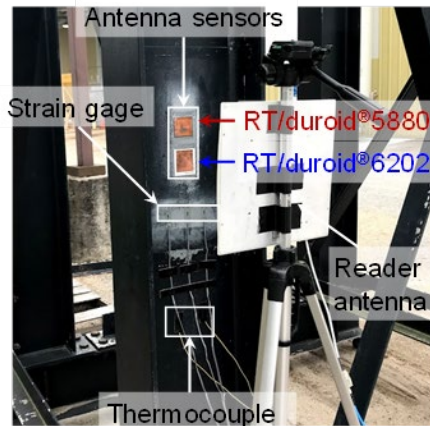
**Fig. 3-5 Resonance frequency change during temperature fluctuation (RT/duroid® 5880 substrate)**

### 3.1.1.2 Outdoor test

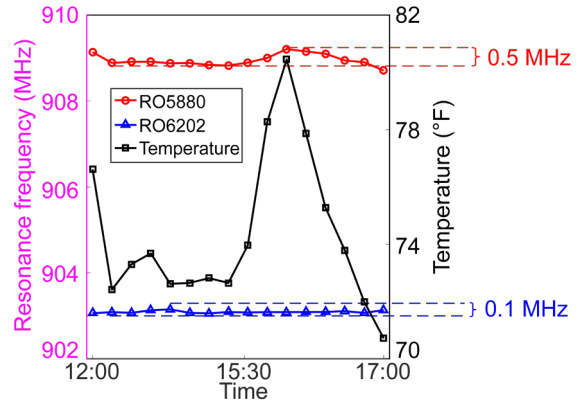
A day-long outdoor temperature test is conducted to study the influence of the temperature fluctuation on the resonance frequency of the antenna sensors. Fig. 3-6(a) shows the outdoor experiment setup. Two antenna sensors, one with RT/duroid® 5880 substrate and the other with RT/duroid® 6202 substrate, are installed on the web surface of a steel I-section column. Metal foil strain gauges are installed to measure the temperature-induced strain on the steel column surface. To keep track of temperature fluctuations in the field, two thermocouples are installed near the sensors. A reader antenna is placed 12 in. from the antenna sensor for wireless interrogation.

The outdoor test starts at noon with environmental temperature at around 76 °F. The temperature is measured every 20 minutes until 17:00 PM. The temperature fluctuation is plotted in Fig. 3-6(b). The highest temperature is around 80 °F and the lowest temperature is around 70 °F. At each time step, interrogation power threshold is measured for both patch antenna sensors. To reduce measurement noise, the reader antenna sweeps the target frequency span five times for each measurement. Resonance frequency changes of both patch antenna sensors are extracted from the average interrogation power

threshold curves and shown in Fig. 3-6(b). A total of about 0.5 MHz resonance frequency change is observed on patch antenna sensor with RT/duroid® 5880 substrate during the test. Meanwhile, the patch antenna sensor with RT/duroid® 6202 substrate shows a total about 0.1 MHz resonance frequency change, which is significantly less than the previous design with RT/duroid® 5880 substrate.



(a) Experiment setup



(b) Resonance frequency change

Fig. 3-6 Outdoor temperature test

### 3.1.2 Mechanical parameter updating

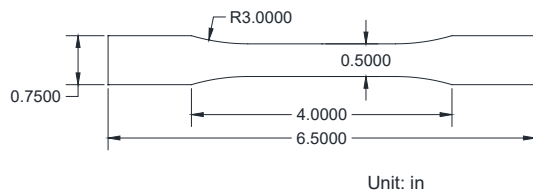
Mechanical properties of the substrate material and the adhesive are studied. A number of tensile tests have been performed to provide baseline data for calibrating the mechanical model parameters.

#### 3.1.2.1 Tensile test for substrate

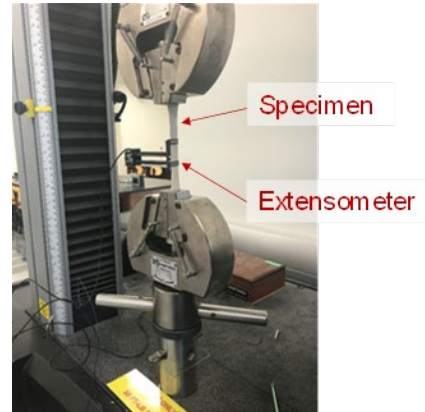
In this section, the nonlinear behavior of the RT/duroid® 6202 substrate sheet is investigated. To characterize mechanical properties of the material along longitudinal and transverse directions, two specimens are fabricated following the ASTM standard [4]. The dimension of the specimen is 6.5 in. × 0.75 in. × 0.031 in., as shown in Fig. 3-7(a). Specimens are mounted on a 2.25-kip Instron 5566 tensile frame



(Fig. 3-7(b)). In the tensile testing, strain data is measured by an extensometer. The loading rate is 1,000  $\mu\epsilon/\text{min}$  and strain is applied up to 10,000  $\mu\epsilon$ .



(a) Schematic of substrate specimen



(b) Experimental setup

**Fig. 3-7 Tensile test for substrate**

A phenomenological model is used to describe the constitutive relationships of the substrate along two directions. A phenomenological model is a mathematical model which describes empirical observations of phenomena such as experimental results. Although the phenomenological model is not directly derived from fundamental theory, the model attempts to describe actual behaviors through key parameters. In the stress-strain relationship of materials, the primary advantage of the phenomenological model is that it remains conceptually simple while offering accuracy comparable with the more sophisticated material models. Furthermore, the model is computationally efficient, and easy to implement in a finite element program. In this project, the Menegotto-Pinto phenomenological model [5, 6] is proposed for describing mechanical properties of the dielectric substrate. The general form of the Menegotto-Pinto model is as follows:

$$\frac{\sigma(\varepsilon)}{\sigma_0} = b \frac{\varepsilon}{\varepsilon_0} + d(\varepsilon) = b \frac{\varepsilon}{\varepsilon_0} + \frac{(1-b) \frac{\varepsilon}{\varepsilon_0}}{\left[1 + \left(\frac{\varepsilon}{\varepsilon_0}\right)^n\right]^{\frac{1}{n}}} \quad (3.2)$$

where  $b$  is the ratio of the final to initial tangent stiffness;  $d$  is the nonlinear portion of the normalized stress at strain  $\varepsilon$  and  $d'$  is the value of  $d$  evaluated at  $\varepsilon_0$ ;  $\sigma_0$  (neither yielding nor ultimate stress) is the normalized stress factor;  $\varepsilon_0$  (neither yielding nor ultimate strain) is the normalized strain factor; it should be noted that both  $\sigma_0$  and  $\varepsilon_0$  are obtained from the intersection point from initial and final tangent curve;  $n$  describes nonlinearity of a stress-strain curve, which is calculated at  $\varepsilon/\varepsilon_0 = 1$ :

$$n = \frac{\log 2}{\log(1-b) - \log d'} \quad (3.3)$$

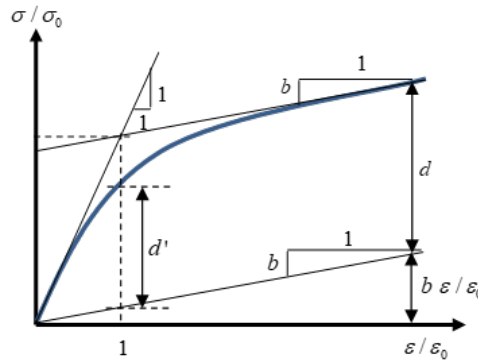


Fig. 3-8 Menegotto and Pinto phenomenological model [5]

To obtain an accurate Menegotto-Pinto model for the dielectric substrate material along each direction,  $\mathbf{x} = [b, n, \varepsilon_0, \sigma_0]$  are chosen as the updating variables. The optimization problem for model updating is formulated as:

$$\begin{aligned} & \underset{\mathbf{x}}{\text{minimize}} && \sum_{i=1}^m [\sigma_{\text{Exp}}(\varepsilon_i) - \sigma_{\text{Cal}}(\varepsilon_i, \mathbf{x})]^2 \\ & \text{subject to} && \mathbf{x}_L \leq \mathbf{x} \leq \mathbf{x}_U \end{aligned} \quad (3.4)$$

where  $m$  is the number of strain steps;  $\sigma_{\text{Exp}}(\varepsilon_i)$  is stress at strain  $\varepsilon_i$  measured from the experiment;  $\sigma_{\text{Cal}}(\varepsilon_i, \mathbf{x})$  is stress at strain  $\varepsilon_i$  calculated from the Menegotto-Pinto model using parameter  $\mathbf{x}$ ;  $\mathbf{x}_L$  and  $\mathbf{x}_U$  are (element-wise) lower and upper bounds of the updating vector parameter  $\mathbf{x}$ .

In the substrate model updating for property along the longitudinal direction, the initial values of the updating variables are defined as:

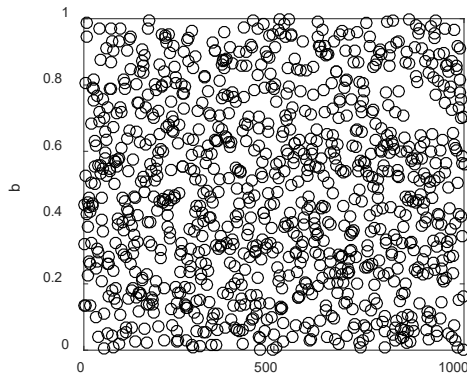
$$\mathbf{x}_0 = [0.5, \quad 2.5, \quad 0.05, \quad 5,500] \quad (3.5)$$

Lower and upper bounds of parameters are empirically set as:

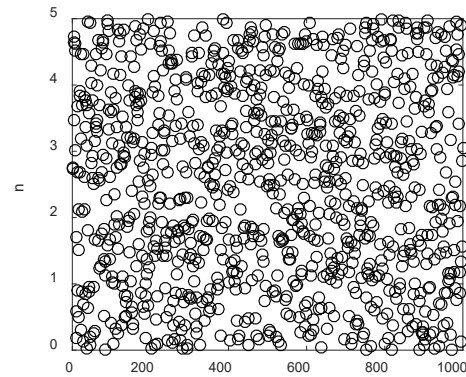
$$\mathbf{x}_L = [0.0, \quad 0.0001, \quad 0.005, \quad 1,000] \quad (3.6)$$

$$\mathbf{x}_U = [1.0, \quad 5.0, \quad 0.1, \quad 10,000] \quad (3.7)$$

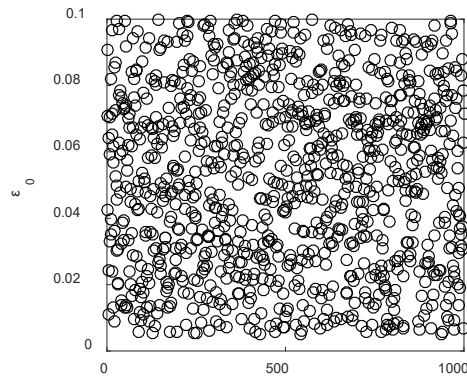
As a global optimization solver, `MultiStart` in the MATLAB optimization toolbox is adopted to solve this model updating problem for substrate mechanical property. Using `MultiStart`, 1,000 trial sets of starting values for the updating variables ( $\mathbf{x}_0 = [b, n, \varepsilon_0, \sigma_0]$ ) are randomly and uniformly generated between the lower bound and the upper bound. Fig. 3-9 shows the starting values for updating substrate constitutive relationship along longitudinal direction.



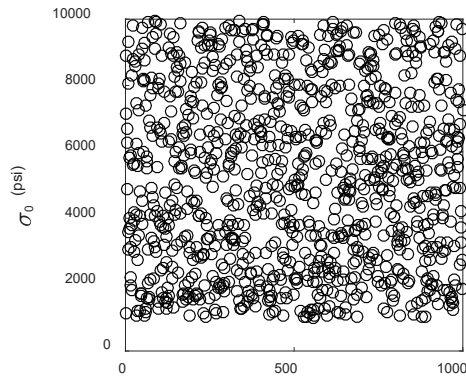
(a) Parameter  $b$



(b) Parameter  $n$



(c) Parameter  $\epsilon_0$

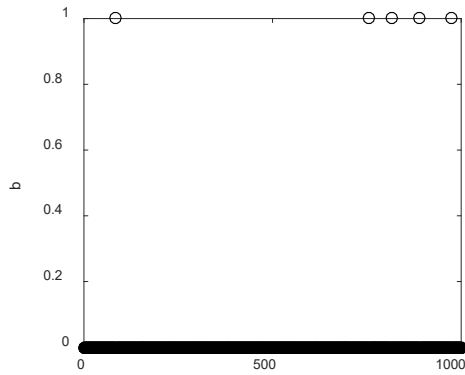


(d) Parameter  $\sigma_0$

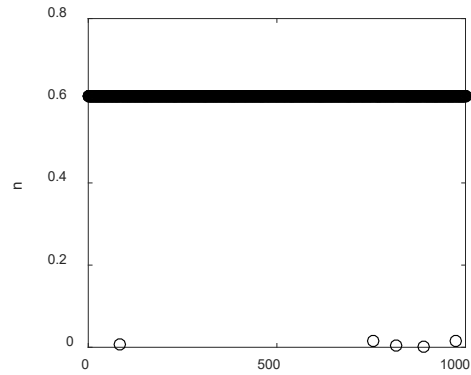
**Fig. 3-9 Starting values for updating substrate constitutive relationship along longitudinal direction**

Starting from each of 1,000 points, the MATLAB command 'lsqnonlin' with the trust region reflective algorithm finds a local optimum. Fig. 3-10 plots the corresponding 1,000 set of optimized values of each parameter. The plot shows that almost all the optimization processes converge at the same values. The optimized values for parameter  $b$ ,  $n$ ,  $\epsilon_0$  and  $\sigma_0$  are  $2 \times 10^{-14}$ , 0.61, 0.02, and 10,000 respectively.

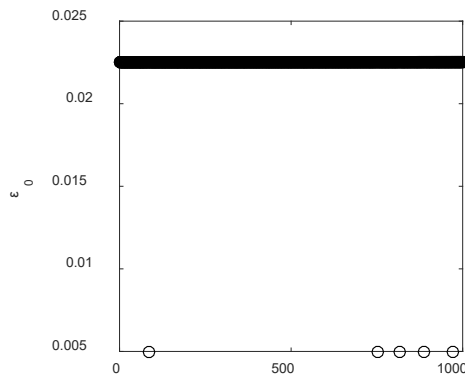
Fig. 3-11 plots stress-strain relationship along longitudinal direction of the experimental, initial, and optimized results. After the model updating procedure, the numerical model matches well with the experimental result.



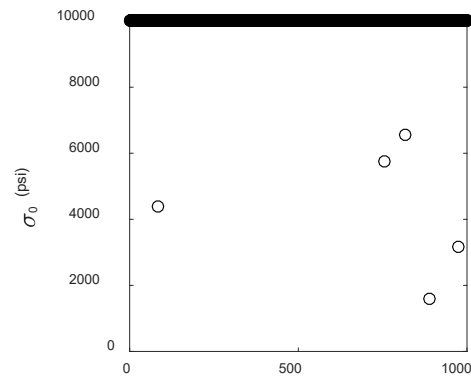
(a) Parameter  $b$



(b) Parameter  $n$



(c) Parameter  $\epsilon_0$



(d) Parameter  $\sigma_0$

**Fig. 3-10 Optimization results for updating substrate constitutive relationship along longitudinal direction**



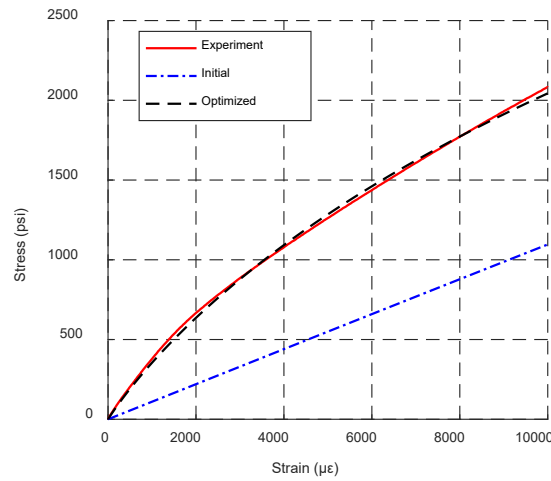
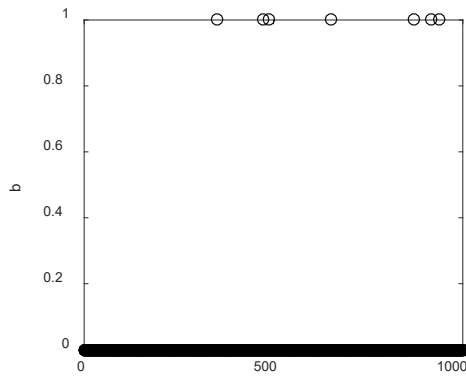
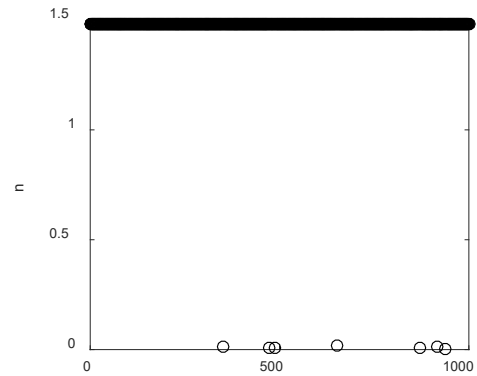


**Fig. 3-11 Constitutive relationship along longitudinal direction**

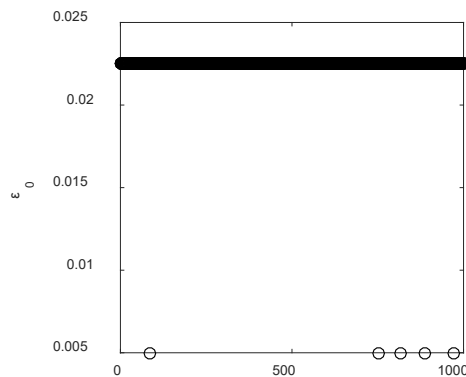
The same model updating procedure is conducted for a constitutive relationship of dielectric substrate along transverse direction. For transverse direction updating, the initial model parameters  $\mathbf{x}_0$  and bounds are the same as longitudinal direction updating (Eq. (3.5), Eq. (3.6), and Eq. (3.7)). Again, the search starts from 1,000 sets of randomly generated values. The corresponding optimized sets of values are shown in Fig. 3-12. Except for six searches, all the other optimization processes converge at the same set of final values. The optimized values for parameters  $b$ ,  $n$ ,  $\varepsilon_0$  and  $\sigma_0$  are  $2 \times 10^{-14}$ , 1.48, 0.03, and 10,000 respectively.



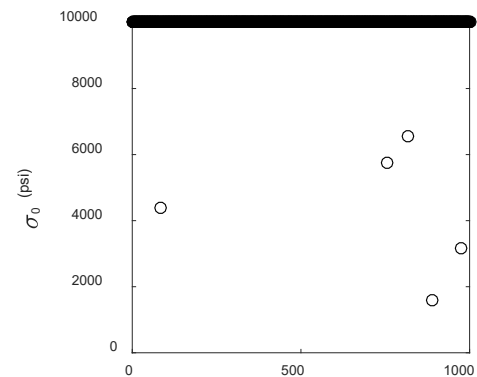
(a) Parameter  $b$



(b) Parameter  $n$



(c) Parameter  $\epsilon_0$



(d) Parameter  $\sigma_0$

**Fig. 3-12 Optimization results for updating substrate constitutive relationship along longitudinal direction**

Fig. 3-13 plots stress-strain relationship along the transverse direction of the experimental, initial, and optimized results. After model updating, the numerical model matches well with the experimental result; the two curves appear to coincide in the figure.

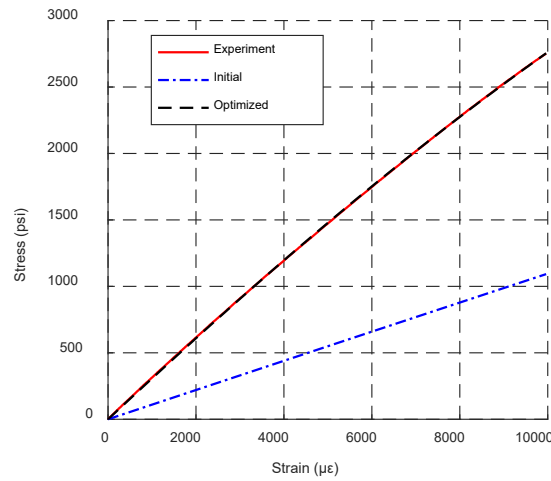


Fig. 3-13 Constitutive relationship along transverse direction

### 3.1.2.2 Strain transfer ratio

To measure the structural strain, the antenna sensor is bonded on the surface of the base structure. Due to adhesive effect between the antenna sensor and the structural surface, only partial strain can be transferred from the structure to the antenna sensor. In order to investigate the nonlinear mechanical behavior of strain transfer ratio for the antenna sensor, a dog-bone aluminum specimen is fabricated. Fig. 3-14 shows the schematic of the aluminum specimen and the substrate patch.

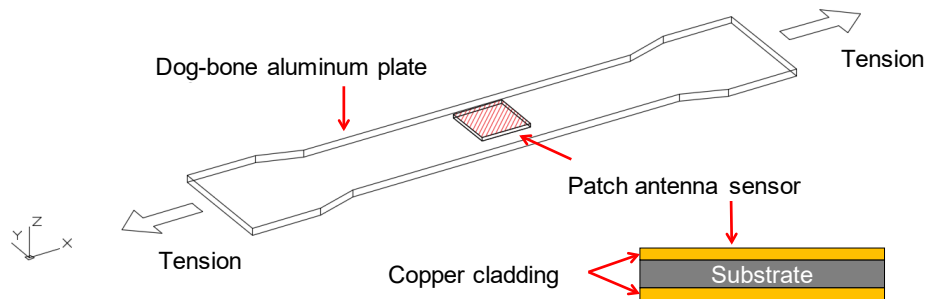


Fig. 3-14 Schematic of an aluminum plate and a substrate patch

To quantify the strain transfer from the specimen to the top of copper cladding, a nonlinear tensile test is conducted. Fig. 3-15 shows the experimental setup for the strain transfer ratio test. Five metal foil strain gauges are installed near the center of the aluminum tensile specimen, for measuring the axial strain on the aluminum specimen. Another six strain gauges are installed on the top copper cladding, for measuring the strain transferred to the top surface. For installation of strain gauges and the substrate patch, M-Bond 610 strain gauge adhesive (Vishay Precision Group, Inc.) is applied. The aluminum specimen is mounted on the MTS 810 testing machine. Starting from zero strain to  $6,000\mu\epsilon$ , 61 strain levels are applied. The test results are shown in Fig. 3-16. For every data point, the horizontal-axis value is the average measurement among strain gauges on the aluminum plate; the vertical-axis value is the average measurement among gauges on the patch antenna sensor. For reference, a 45-degree line is drawn on the plot. When the strain level is less than  $3,000\mu\epsilon$ , the difference between horizontal and vertical-axis values is small, which proves that with current sensor geometry and substrate material, strain/deformation in the aluminum specimen can be properly transferred to the top copper layer. After  $3,000\mu\epsilon$ , the percentage of strain transferred from the aluminum plate to the patch antenna sensor decreases as the applied strain increases.

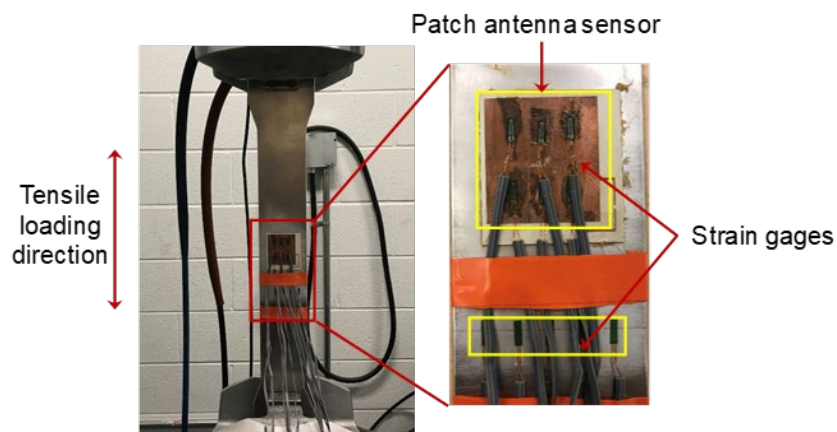
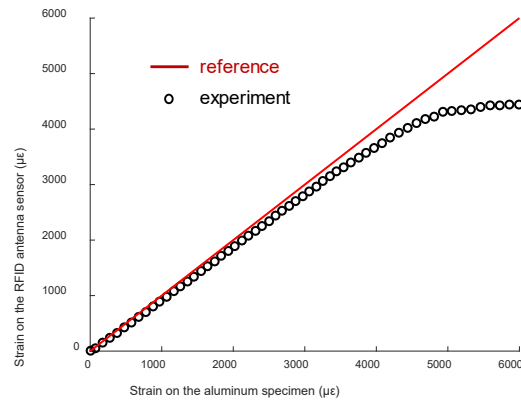
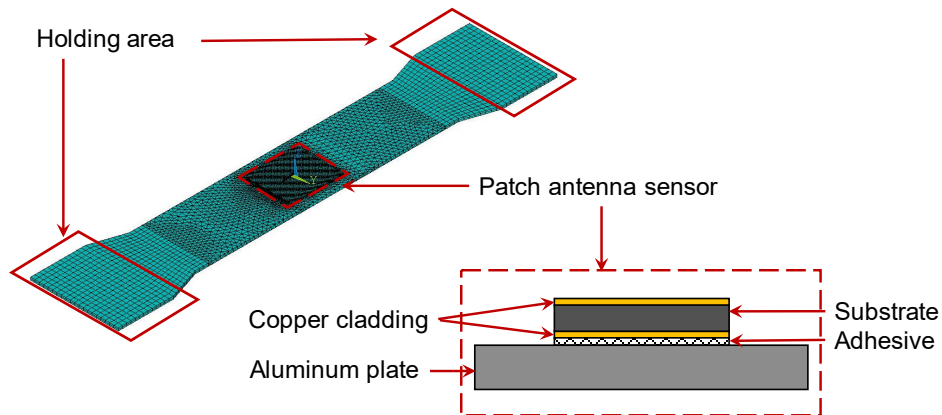


Fig. 3-15 Experimental setup for strain transfer ratio test



**Fig. 3-16 Strain on the patch antenna sensor versus strain on the aluminum plate**

The strain transfer ratio is dependent on mechanical properties of the adhesive between the patch antenna sensor and the aluminum plate. The Menegotto-Pinto phenomenological model is used to describe the mechanical properties of the adhesive layer. To update the parameters in the model, a 3D finite element (FE) model is built (Fig. 3-17). Nonlinear constitutive relationships are used for the aluminum, copper, and substrate to achieve accurate simulation.



**Fig. 3-17 Finite element model for strain transfer ratio simulation**

The optimization problem for updating parameters  $\mathbf{x} = [b, n, \varepsilon_0, \sigma_0]$  of the adhesive is formulated as:

$$\begin{aligned} & \underset{\mathbf{x}}{\text{minimize}} && \sum_{i=1}^m [T_{\text{Exp}}(\varepsilon_i) - T_{\text{FEM}}(\varepsilon_i, \mathbf{x})]^2 \\ & \text{subject to} && \mathbf{x}_L \leq \mathbf{x} \leq \mathbf{x}_U \end{aligned} \tag{3.8}$$

where  $m$  is the number of strain steps used for model updating;  $\varepsilon_i$  is strain level at  $i$ -th step;  $T_{\text{Exp}}(\varepsilon_i)$  is strain transfer ratio at strain step  $\varepsilon_i$  obtained from the experiment;  $T_{\text{FEM}}(\varepsilon_i, \mathbf{x})$  is transfer ratio at strain step  $\varepsilon_i$  calculated from the FE model;  $\mathbf{x}_L$  and  $\mathbf{x}_U$  are lower and upper bounds.

The initial values of the updating variables are chosen as:

$$\mathbf{x}_0 = [0.206, \quad 4.122, \quad 1.58 \times 10^{-4}, \quad 2.00 \times 10^3] \tag{3.9}$$

Lower and upper bounds of parameters are empirically set as:

$$\mathbf{x}_L = [0.0, \quad 0.0, \quad 10^{-5}, \quad 10^{-3}] \tag{3.10}$$

$$\mathbf{x}_U = [1.0, \quad 20, \quad 0.1, \quad 10^4] \tag{3.11}$$

The optimization problem is solved by the Covariance Matrix Adaptation Evolution Strategy (CMA-ES) algorithm [7]. The optimized values for parameters are solved as:

$$\mathbf{x}^* = [0.023, \quad 6.369, \quad 3.46 \times 10^{-5}, \quad 9.94 \times 10^3] \tag{3.12}$$

Fig. 3-18 plots strain transfer ratio of the experimental, initial, and optimized results. After model updating, the numerical model matches similarly with the experimental result.

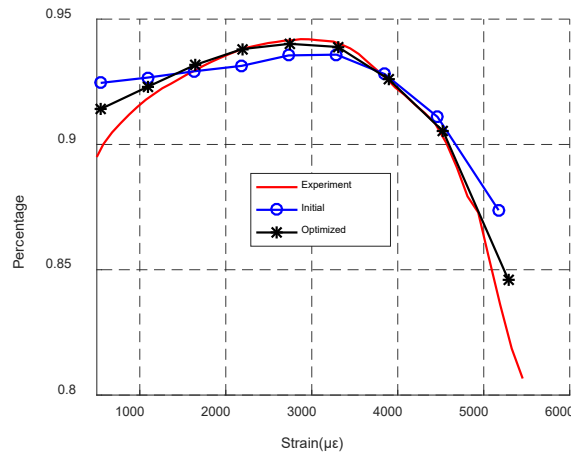


**Fig. 3-18 Strain transfer ratio**

### 3.1.3 Electromagnetic parameter updating

To investigate the variation of dielectric constant caused by strain effect, a 925 MHz transmission-line resonator (Fig. 3-19) is designed based on the ASTM standard D3380-10 [8]. The resonator consists of top microstrip copper lines which are separated from the bottom copper ground plane by the 31-mil Rogers RT/duroid® 6202 substrate. The 925 MHz resonance frequency requires the length of the center microstrip line to be 100 mm. The resonance frequency can be experimentally measured by identifying the peak of the transmission coefficient ( $S_{21}$ ) curve:

$$S_{21}(f) = \frac{V_2^{\text{Out}}(f)}{V_1^{\text{Input}}(f)} \quad (3.13)$$

Here  $V_1^{\text{Input}}$  is the incident voltage from Port 1 at certain frequency  $f$ ;  $V_2^{\text{Out}}$  is the output voltage from Port 2 at the same electromagnetic frequency at the input frequency  $f$ .



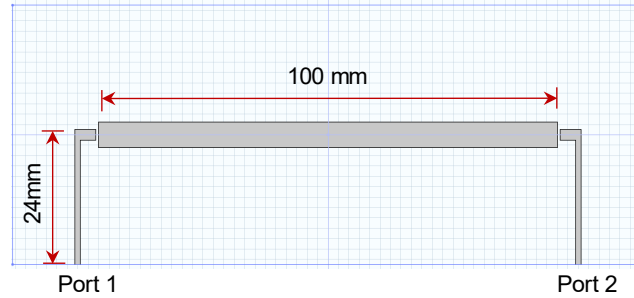
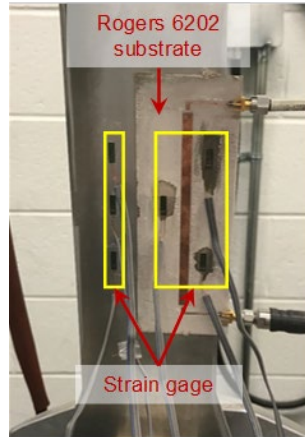
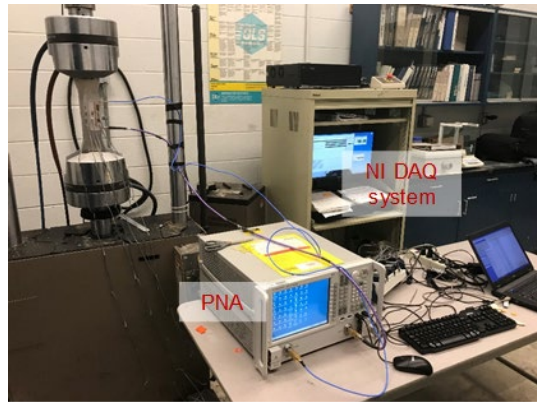


**Fig. 3-19 Transmission line design**

Given constant input power, the maximum output power is transferred from Port 1 to Port 2 at resonance frequency. The peak of the  $S_{21}$  curve of the transmission-line resonator corresponds to the resonance frequency of the resonator. To characterize strain effect on dielectric constant change, a tensile test for the transmission-line resonator is conducted. Experimental setup is shown in Fig. 3-20. Three strain gauges are installed on the aluminum specimen another three strain gauges are installed on the substrate (Fig. 3-20(a)). A National Instruments strain gauge module (NI 9235), with a CompactDAQ Chassis (NI cDAQ-9172), is used for collecting data from metal foil strain gauges. The axial force is applied by the MTS 810 testing machine (Fig. 3-20(b)). Two ports of the transmission-line resonator are connected to an Agilent Technologies Professional Network Analyzer (N5222A) to measure the  $S_{21}$  parameter curve. A  $100\mu\epsilon$  strain increment is achieved at each loading step till around  $6,000\mu\epsilon$ . For clarity,  $S_{21}$  curves with only seven strain levels are plotted in Fig. 3-21(a). The resonance frequency (the maximum peak point) clearly shifts towards the left as strain increases. The resonance frequency at each strain level is extracted from the  $S_{21}$  plot and the resonance frequency versus strain plot is shown in Fig. 3-21(b).

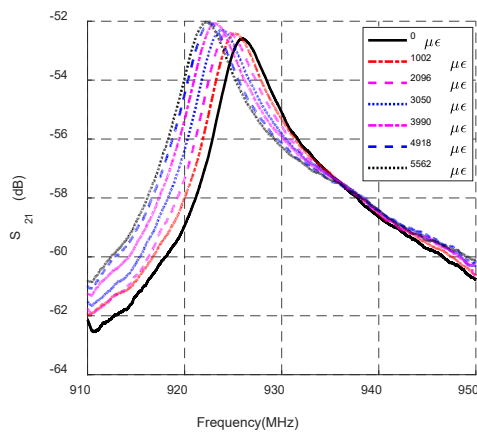


(a) Specimen configuration

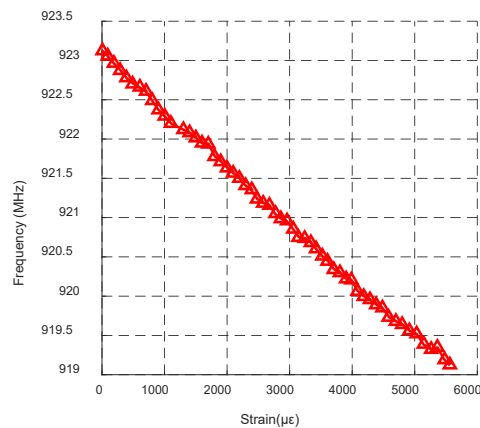


(b) Experimental setup

**Fig. 3-20 Experimental setup for transmission line test**



(a)  $S_{21}$  curve



(b) Resonance frequency versus strain plot

**Fig. 3-21 Transmission line test results**

Electrostriction is defined as the variation of the dielectric properties of a material under mechanical strain [9]. A multi-physics model should consider the electrostriction effect, in order to perform accurate antenna simulation under large strain. The relation between dielectric constant and strain in this transmission line model can be expressed as:

$$\beta = \beta_0 + \alpha_1 \varepsilon + \alpha_2 \varepsilon(1 - 2\nu) \quad (3.14)$$

where  $\beta_0$  is an initial dielectric constant value at zero strain;  $\varepsilon$  is the strain along the transmission line;  $\nu$  is the Poisson's ratio;  $\alpha_1$  and  $\alpha_2$  are electrostriction parameters.

Dielectric constant model updating is conducted to minimize the difference of electrostriction effects between experimental data and numerical solution. The model updating formulation through two optimization values  $\alpha = [\alpha_1, \alpha_2]$  is:

$$\begin{aligned} & \underset{\alpha}{\text{minimize}} \quad \sum_{i=1}^m [f_{\text{Exp}}(\varepsilon_i) - f_{\text{Cal}}(\varepsilon_i, \alpha)]^2 \\ & \text{subject to} \quad \alpha_L \leq \alpha \leq \alpha_U \end{aligned} \quad (3.15)$$

where  $m$  is the number of strain steps;  $\varepsilon_i$  is strain level at  $i$ -th step;  $f_{\text{Exp}}(\varepsilon_i)$  is the resonance frequency at  $\varepsilon_i$  from experimental data;  $f_{\text{Cal}}(\varepsilon_i, \alpha)$  is the resonance frequency at  $\varepsilon_i$  calculated from a scaled transmission line model;  $\alpha_L$  and  $\alpha_U$  are lower and upper bounds of the updating vector parameter  $\alpha$ .

In this model updating problem, `lsqnonlin` in MATLAB optimization toolbox is adopted to solve the optimization problem Eq. (3.15). The initial parameters are chosen as:

$$\alpha_0 = [-0.6, -1] \quad (3.16)$$

Lower and upper bounds are estimated from trial and error, and their ranges are set as:

$$\alpha_L = [-1, -2.5] \quad (3.17)$$

$$\alpha_U = [-0.2, -0.5] \quad (3.18)$$

Solving the optimization problem, optimized values for parameter  $\alpha_1$  and  $\alpha_2$  are calculated as:

$$\alpha^* = [-0.2913, -1.5748] \quad (3.19)$$

Fig. 3-22 shows the updating results for the dielectric constant. When the effect of dielectric constant change under strain is neglected, the discrepancy between experimental and simulated resonance

frequencies is clear. After model updating, the numerical model matches better with the experimental result.

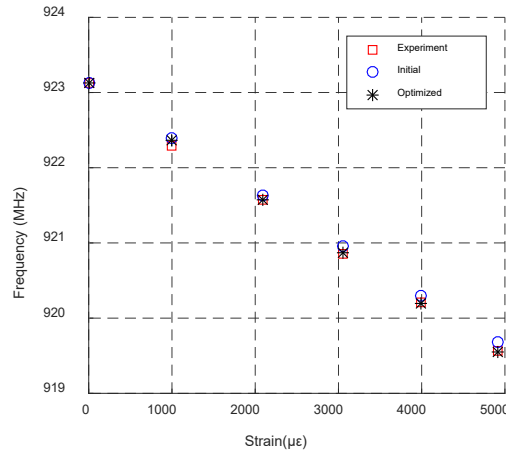


**Fig. 3-22 Updating results for dielectric constant updating**

### 3.2 Multi-physics simulation

To accurately describe both mechanical and electromagnetic behaviors of the patch antenna sensor, a multi-physics coupled simulation approach is adopted. The patch antenna sensor is modeled using ANSYS software package. Fig. 3-23(a) shows the finite element model. The antenna sensor is attached at the center of a tapered aluminum plate. Above the antenna sensor, an air layer is built to consider the fringing effect. Shell elements are utilized to model the copper cladding on both the top and bottom sides of the antenna sensor. Solid elements are utilized to model the substrate layer, the air layer, and the aluminum specimen. For simplicity, the bonding effect between the antenna sensor and the aluminum plate is considered ideal in the simulation, i.e. the bottom copper cladding shares the same finite element nodes with the corresponding area of the top surface at the aluminum plate.

To generate three-point bending in the mechanical simulation, the bottom nodes of the aluminum specimen fix the translational Degree of Freedoms (DOFs) along  $x$ ,  $y$ , and  $z$ . Two corners in the middle part of the aluminum specimen are fixed along  $z$ -direction and free to move in  $x$  and  $y$ . Forces along  $z$ -direction are applied on the top nodes of the aluminum specimen to generate compression strain in the sensor area. From 0 to  $700 \mu\epsilon$  with  $50 \mu\epsilon$  increment, 15 strain levels in total are simulated. Fig. 3-23(b) shows the strain distribution along  $y$ -direction on the antenna sensor at strain level of  $700 \mu\epsilon$ . Approximate uniform strain distribution is achieved on the antenna sensor. After the mechanical simulation at each strain level, the deformed finite element model is used for electromagnetic simulation to calculate the resonance frequency of the antenna sensor. Fig. 3-23(c) illustrates the current pattern on the antenna sensor at its resonant mode. Using this multi-physics simulation approach, the resonance frequency of deformed antenna sensor at each strain level can be accurately calculated. Fig. 3-23(d) plots the resonance frequency change along with the compression strain. Linear regression is applied on these data points, and the strain sensitivity is calculated as  $-865 \text{ Hz}/\mu\epsilon$ .

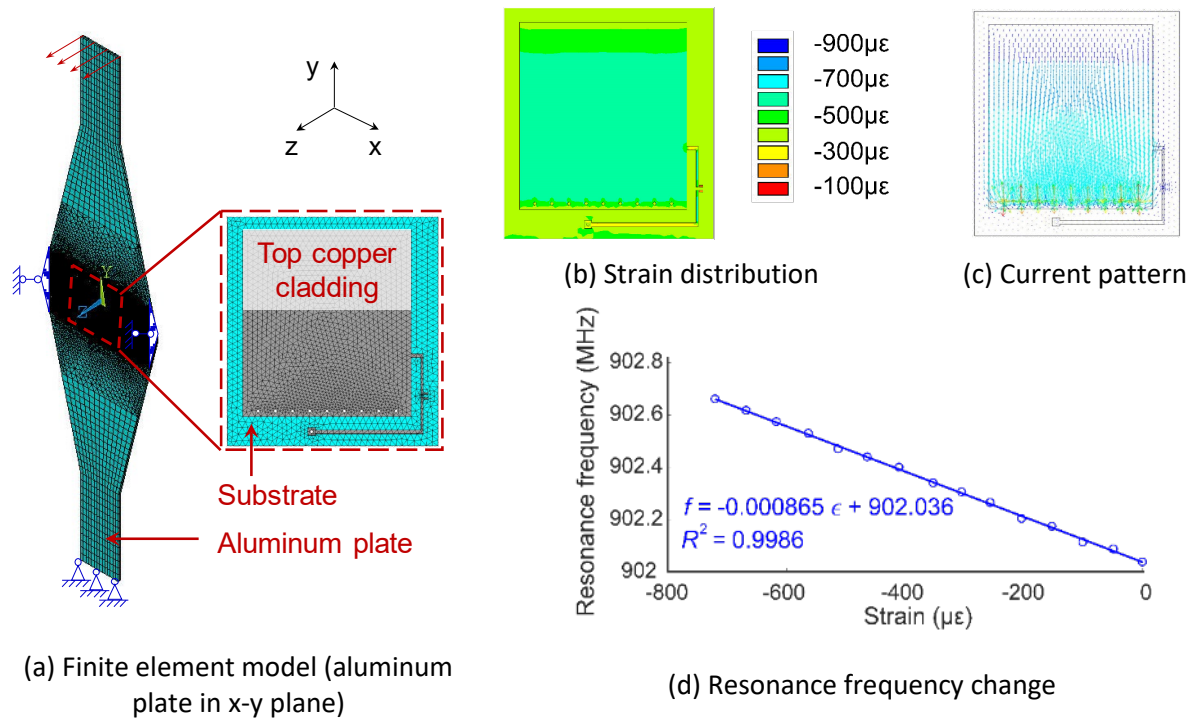


Fig. 3-23 Multi-physics simulation on patch antenna sensor

### 3.3 Strain sensing test

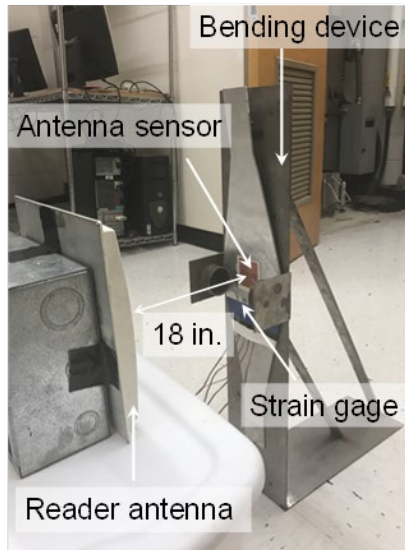
Strain sensing performance of patch antenna sensors is described in this section. Section 3.3.1 presents the strain sensing results from a laboratory compression test. Due to the limited size of the specimen, only the RFID patch antenna sensor is tested through the compressive test. Section 3.3.2 shows the tensile strain sensing tests of both the RFID patch antenna sensor and the dual-mode RFID patch antenna sensor.

#### 3.3.1 Compressive test

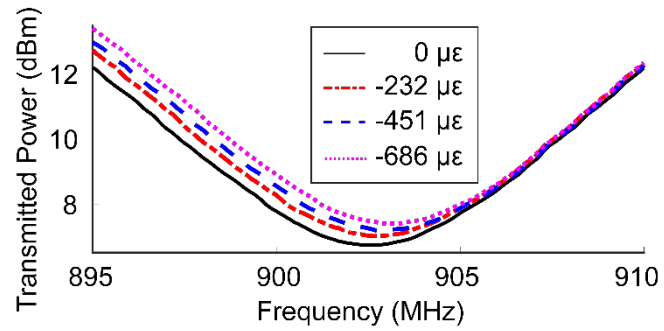
A laboratory compression test is conducted to investigate the strain sensing performance of the patch antenna sensor. Fig. 3-24(a) shows the setup of the compression test. A three-point bending device is designed and utilized to apply compression strain on the patch antenna sensor. The patch antenna sensor

and reference metal foil strain gauges are installed in the middle of a tapered aluminum specimen. Due to limited space in the sensing area, the compressive test is only conducted on the RFID patch antenna sensor. The interrogation distance between the patch antenna sensor and the reader antenna is set as 18 in. From 0 to 700  $\mu\epsilon$ , the load is adjusted so that approximately a 50  $\mu\epsilon$  increment is obtained at each loading step. The interrogation power threshold of the patch antenna sensor is measured at each loading step. To reduce measurement noise, five frequency sweeps are conducted for each measurement. The average interrogation power threshold are plotted in Fig. 3-24(b). For clarity, only four representative strain levels are shown. Resonance frequency of the patch antenna sensor at each strain level is then determined by the peak picking of each average interrogation power threshold curve. As expected, the resonance frequency increases as the compression strain increases. Fig. 3-24(c) plots the resonance frequency change with the strain. Linear regression is applied on these data points, and the strain sensitivity is calculated as  $-874 \text{ Hz}/\mu\epsilon$ , which is close to the simulated result  $-865 \text{ Hz}/\mu\epsilon$  as shown in Section 3.2. In addition, the coefficient of determination is 0.9945, confirming the approximate linear relationship between frequency change and strain.

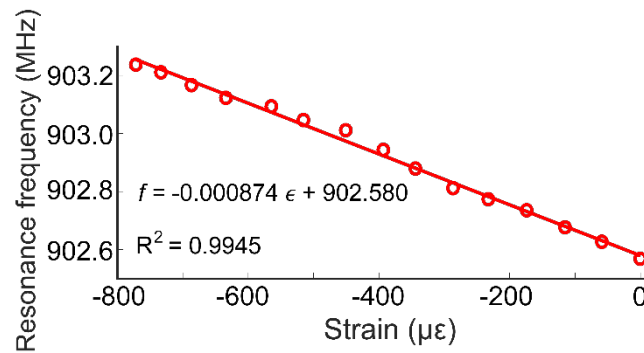




(a) Experiment setup



(b) Interrogation power threshold



(c) Resonance frequency change

Fig. 3-24 Compression test

### 3.3.2 Tensile test

#### 3.3.2.1 RFID patch antenna sensor

Laboratory tensile testing is conducted to investigate the strain sensing performance of the RFID patch antenna sensor. The patch antenna sensor and reference metal foil strain gauges are installed in the middle of an aluminum specimen. The interrogation distance between the patch antenna sensor and the reader antenna is set as 12 in. From 0 to about 330  $\mu\epsilon$ , seven loading steps are tested to investigate the relationship between the applied strain and resonance frequency of the antenna sensor.



**Fig. 3-25 Experimental setup for tensile testing**

The interrogation power threshold of the patch antenna sensor is measured at each loading step. To reduce measurement noise, five frequency sweeps are conducted for each measurement. The average interrogation power threshold are plotted in Fig. 3-26(a). Resonance frequency of the patch antenna sensor at each strain level is then determined by the peak picking of each average interrogation power threshold curve. As expected, the resonance frequency decreases as the tensile strain increases. Fig. 3-26(b) plots the resonance frequency change with strain. Linear regression is applied on these data points, and the strain sensitivity is calculated as  $-521 \text{ Hz}/\mu\epsilon$ . In addition, the coefficient of determination is 0.9909, confirming the approximately linear relationship between frequency change and strain.

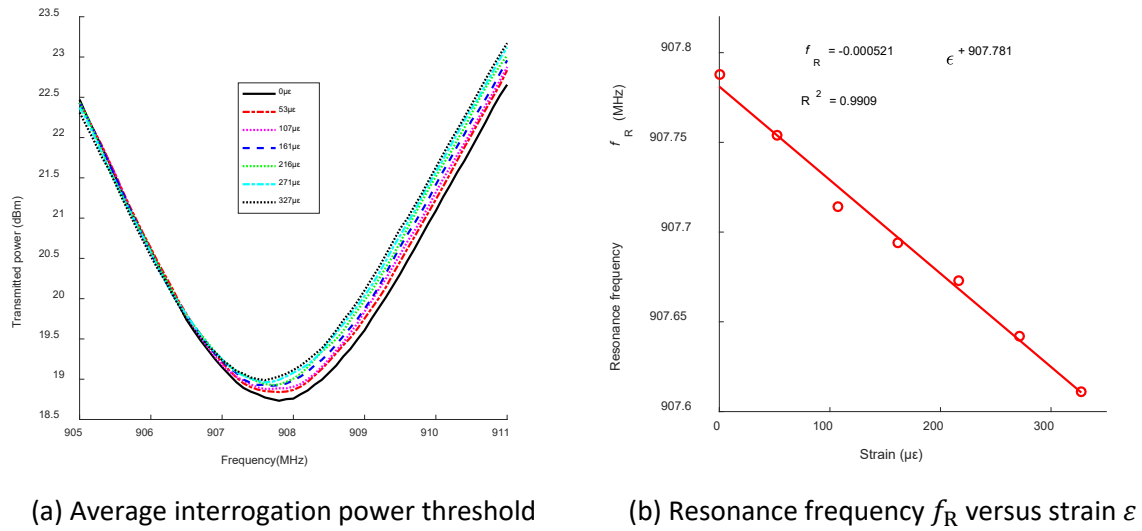
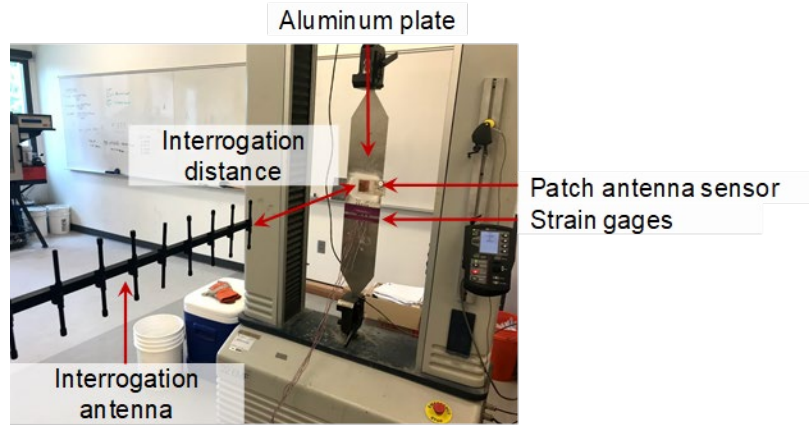


Fig. 3-26 Tensile test results

### 3.3.2.2 Dual-mode RFID patch antenna sensor

A laboratory tensile test is conducted to investigate the strain sensing performance of the dual-mode RFID patch antenna sensor. The dual-mode patch antenna sensor and reference metal foil strain gauges are installed in the middle of an aluminum specimen. The interrogation distance between the patch antenna sensor and the reader antenna is set as 36 in for passive mode testing and 60 in for active mode testing. From 0 to about 320  $\mu\epsilon$ , seven loading steps are tested to investigate the relationship between applied strain and the resonance frequency of antenna sensor.



**Fig. 3-27 Experimental setup for tensile testing**

**(1) Passive mode test**

The passive mode test is conducted first. The interrogation power threshold of the patch antenna sensor is measured at each loading step. To reduce measurement noise, five frequency sweeps are conducted at each step for taking the average. The average interrogation power threshold curves at each of the seven loading steps/strain levels are plotted in Fig. 3-28(a). Resonance frequency of the patch antenna sensor at each strain level is then determined by peak picking of each average interrogation power threshold curve. As expected, the resonance frequency decreases as the tensile strain increases. Fig. 3-28(b) plots the resonance frequency change with the strain. Linear regression is applied on these data points, and the strain sensitivity is calculated as  $-599 \text{ Hz}/\mu\epsilon$ . In addition, the coefficient of determination is 0.9871, confirming the approximately linear relationship between frequency change and strain.

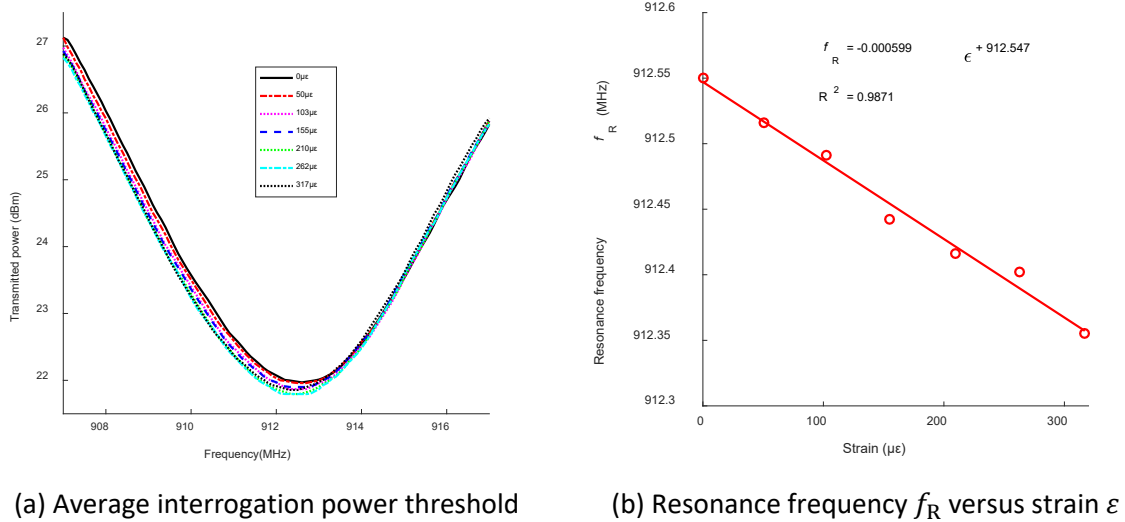


**Fig. 3-28 Passive mode tensile test results**

**(2) Active mode test**

The active mode test is conducted next and the interrogation distance is set as 60 in. To reduce measurement noise, again five frequency sweeps are conducted for each interrogation power threshold measurement. The average interrogation power threshold curves at seven strain levels are plotted in Fig. 3-29(a). Resonance frequency of the patch antenna sensor at each strain level is then determined by the peak picking of each average interrogation power threshold curve. As expected, the resonance frequency decreases as tensile strain increases. Fig. 3-29(b) plots the resonance frequency change with strain. Linear regression is applied on these data points, and the strain sensitivity is calculated as  $-582 \text{ Hz}/\mu\epsilon$ . In addition, the coefficient of determination is 0.9787, confirming the approximately linear relationship between frequency change and strain.

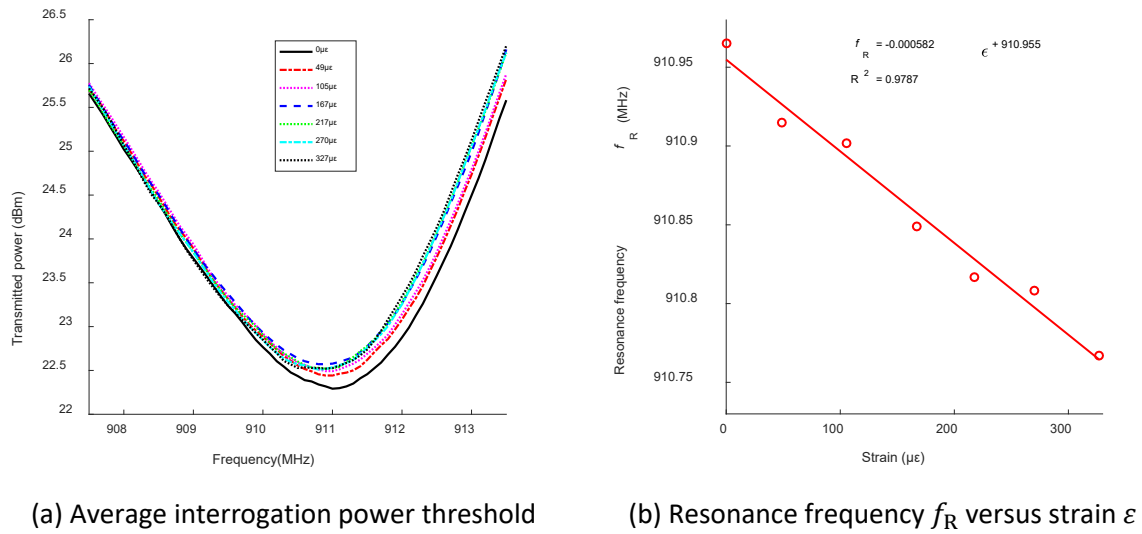


Fig. 3-29 Active mode tensile test results

### 3.4 Crack sensing test

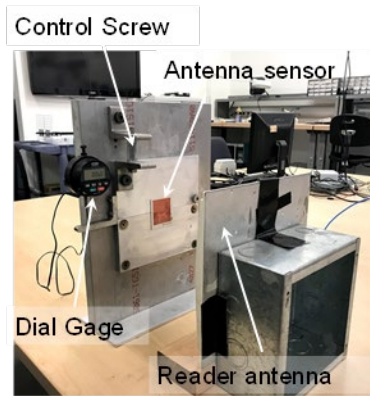
Crack sensing performance of the patch antenna sensor is described in this section. Section 3.4.1 presents the crack sensing results through an emulated crack test. Section 3.4.2 shows the crack sensing results through a fatigue crack test.

#### 3.4.1 Emulated crack test

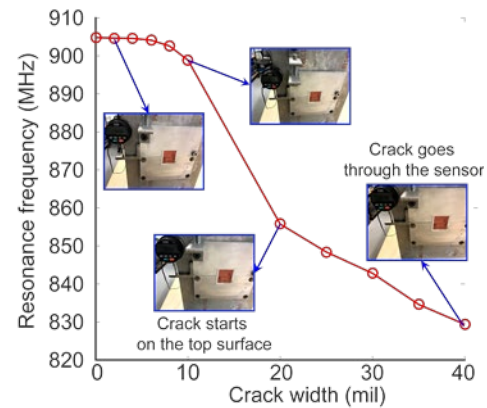
To conveniently emulate crack propagation, a special crack testing device (Fig. 3-30 (a)) is designed for the experiments. The crack testing device consists of three aluminum plates, i.e. a base plate, a rotating top plate, and a fixed bottom plate. Due to their thickness, all three plates can be assumed to remain rigid during crack testing for the sensor. The fixed bottom plate is fastened to the base plate by four corner bolts. The rotating top plate is attached to the base plate by one bolt at the bottom right corner, which acts as the rotation axis. A fine-resolution displacement control screw is installed at the top left corner of the rotating plate. By turning the screw, a rotation is imposed on the top plate and a crack/gap is opened

between the top and bottom plates. The crack opening size is measured by a digital dial gauge (0.0001 in. resolution) mounted at the left side of the base plate. A spring-loaded probe from the gauge pushes against an angle bracket which is fastened to the left edge of the rotating plate.

For crack sensing, the antenna sensor is bonded on the rotating and fixed plates, above the gap and at the center of the crack opening line, as shown in Fig. 3-30(a). The panel reader antenna faces the center of the prototype sensor at a distance of 12 in. Through a coaxial cable, the reader antenna is connected with the Tagformance reader unit. At each gap opening size, the Tagformance reader sweeps through a frequency range to measure the interrogation power threshold, so that the resonance frequency of the antenna sensor can be determined. After the reader finishes interrogation at one gap opening size, the displacement control screw is turned to reach the next gap opening size.



(a) Experiment setup



(b) Resonance frequency change

**Fig. 3-30 Emulated crack test**

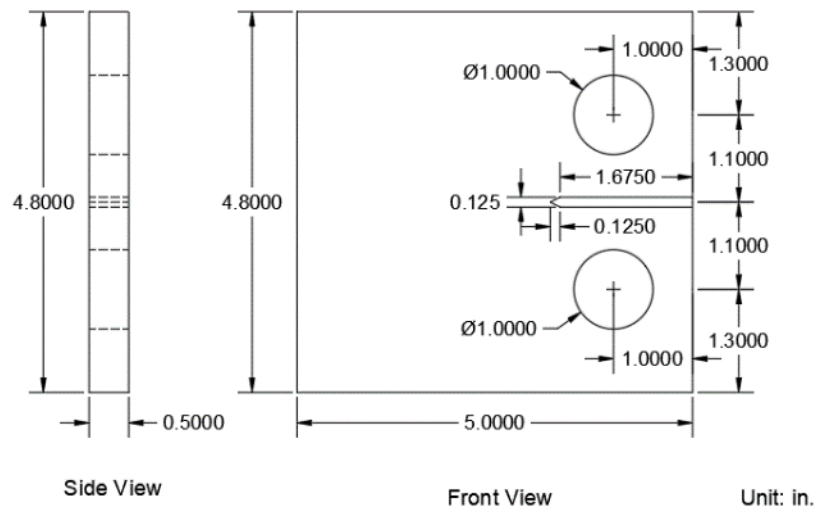
In total, eleven gap opening sizes are wirelessly measured during the experiment. The resonance frequencies extracted from interrogation power curves are plotted in Fig. 3-30(b). For clarity, only four representative photos of the deformed/cracked antenna sensor are shown in the plot. No fracture but slight deformation occurs on the sensor when the gap opening size is smaller than 10 mils (milli-inches).



When the gap opening size is larger than 20 mils, the crack starts to propagate on the top surface of the sensor. After the gap opening size reaches 40 mils, the crack grows through the entire antenna width and no response from the antenna sensor can be received by the Tagformance reader.

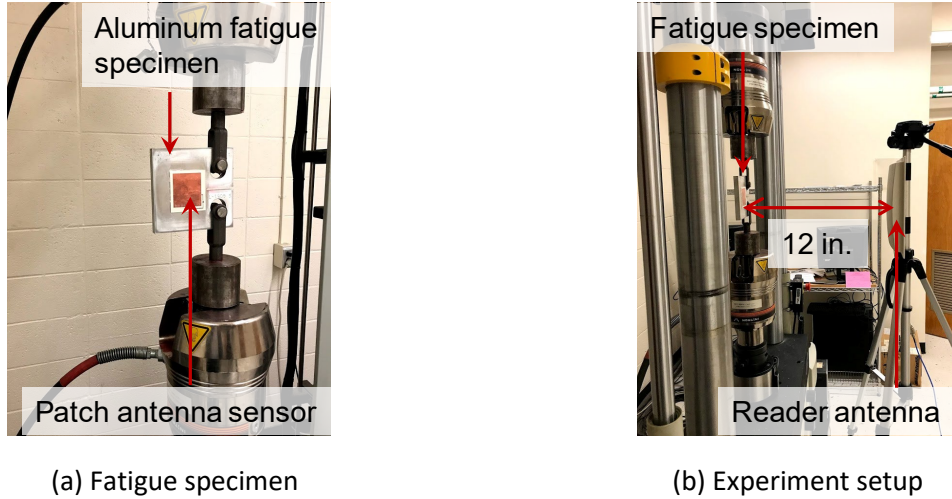
### 3.4.2 Fatigue crack test

To characterize sensor performance measuring fatigue crack growth, a compact-tension (CT) specimen is designed and fabricated according to ASTM standard E647-11 [2]. Fig. 3-31 shows the design drawing of the fatigue specimen.



**Fig. 3-31 Design drawing of fatigue specimen**

To measure the crack propagating on the specimen, a patch antenna sensor is installed in the center area of the specimen. A panel antenna is used as the reader antenna to acquire data from the patch antenna sensor wirelessly. Fig. 3-32 shows the experiment setup for the fatigue test.



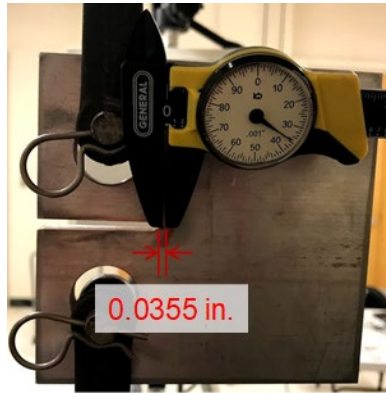
**Fig. 3-32 Experimental setup for the fatigue crack test of patch antenna sensor**

Table 3-1 summarizes the cyclic loading schedule and crack measurement results during fatigue testing. The sinusoidal cyclic loading frequency is set as 5 Hz during the entire test. A crack of 0.0355 in. length is first generated using a larger loading range, oscillating at 2.25 ~ 4.5 kips for 15,000 cycles. After pre-crack, the tensile load oscillates within a smaller range for the following cyclic loading steps, every step consisting of 10,000 cycles. At the end of every step, the loading machine is paused with a static load at 3 kips. The crack length is measured by a caliper. Fig. 3-33 shows representative photos of the specimen after different loading steps.

**Table 3-1 Cyclic loading schedule and crack measurements during the fatigue test**

Test number	Target Setpoint (Kips)	Loading range (Kips)	Frequency (Hz)	Number Of cycles	Crack Length (in.)
Initial	3.0	0.0	--	0	0
Test 1 (Pre-crack)	3.375	2.25~4.5	5	15,000	0.0355
Test 2	3.0	2~4	5	10,000	0.1149
Test 3	3.0	2~4	5	10,000	0.2121
Test 4	3.0	2~4	5	10,000	0.3956
Test 5	3.0	2~4	5	10,000	0.5710
Test 6	3.0	2~4	5	10,000	0.8822

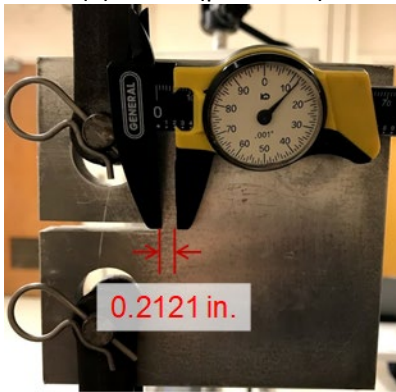
Test 7	3.0	2~4	5	-	-
--------	-----	-----	---	---	---



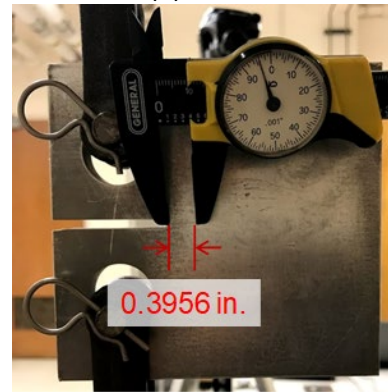
(a) Test 1 (pre-crack)



(b) Test 2



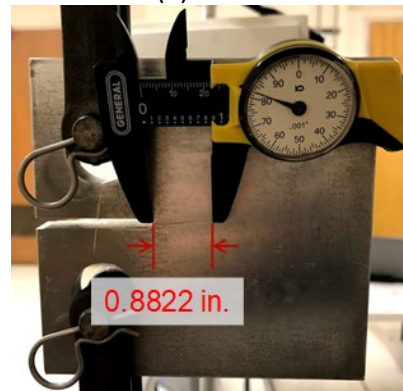
(c) Test 3



(d) Test 4



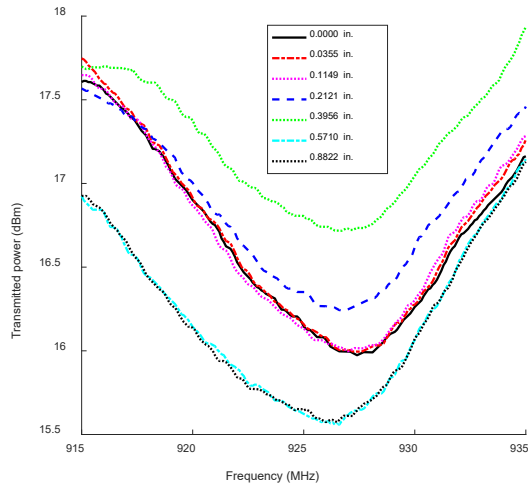
(e) Test 5



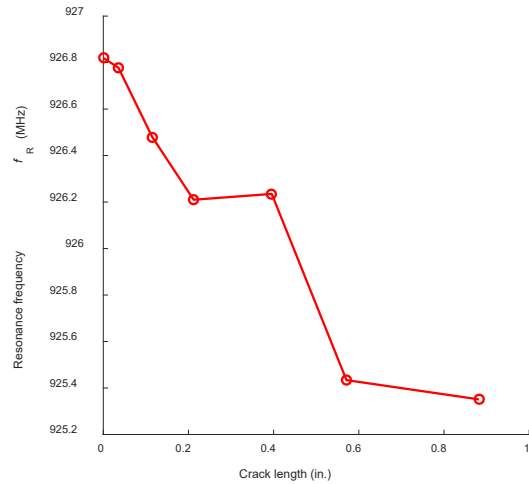
(f) Test 6

Fig. 3-33 Crack propagation in the fatigue specimen

The test continues until the specimen breaks apart into two pieces, which occurs during loading step #7. Interrogation power threshold of the patch antenna sensor is wirelessly measured immediately after each loading step. To reduce environmental noise, five frequency sweeps are performed in the measurement. The average interrogation power threshold at different loading steps are plotted in Fig. 3-34(a). Resonance frequency of the antenna sensor at each loading step is extracted from the interrogation power threshold curve. The resonance frequencies of the antenna sensor during the fatigue test are plotted in Fig. 3-34(b). As expected, the antenna resonance frequency decreases along with the crack propagating across the specimen.



(a) Average interrogation power



(b) Resonance frequency change during temperature fluctuation

**Fig. 3-34 Fatigue test results of the patch antenna sensor**

## 4 FINDINGS

This research improves the performance of novel patch antenna sensors for strain and crack monitoring. The first focus is to reduce the effect of temperature fluctuation on the resonance frequency change of patch antenna sensors. Thermally stable patch antenna sensors have been developed for measuring strain and crack on structures. Secondly, mechanical and electromagnetic properties of the substrate material are investigated through laboratory testing. The characterized material properties are used in multi-physics simulation to accurately describe behaviors of patch antenna sensors. Finally, a dual-mode patch antenna sensor is designed to achieve longer interrogation distance.

### 4.1 Thermal stability

Thermal property of dielectric substrate affects the resonance frequency change of patch antenna sensors. The influence of temperature fluctuation on antenna sensors has been investigated through a chamber test and a day-long outdoor test. Both tests have shown that the RT/duroid® 6202 substrate is much more thermally stable than the RT/duroid® 5880 substrate. In the chamber test, the patch antenna sensor with RT/duroid® 6202 substrate experiences 0.3 MHz change in resonance frequency when the chamber temperature decreases from 123 °F to 37 °F. Alternatively, there is a 5 MHz change in the patch antenna sensor with RT/duroid® 5880 substrate when the temperature changes from 110 °F to 32 °F. In the day-long outdoor test, the patch antenna sensor with RT/duroid® 6202 substrate shows a total about 0.1 MHz resonance frequency change, while the patch antenna sensor with RT/duroid® 5880 substrate shows a total about 0.5 MHz resonance frequency change under the same environmental disturbance.

### 4.2 Material property testing

To investigate the mechanical and electromagnetic properties of the substrate under strain, tensile tests are conducted. The Menegotto-Pinto model is introduced to characterize the constitutive relationships of



the substrate along both longitudinal and transverse directions. The substrate exhibits slight nonlinearity in the strain range from 0 to 10,000  $\mu\epsilon$ . Tensile test on a transmission line indicates that the dielectric constant of the substrate decreases as the strain increases. Numerical optimization is performed to find reasonable parameter values to describe the material properties.

Strain transfer ratio is investigated through the tensile test. Due to shear lag effect, only part of the strain on the base structure can be transferred to the top copper cladding of the antenna sensor. The Menegotto-Pinto model is used to describe the mechanical property of the adhesive between the antenna sensor and the base structure. Model updating is shown to reduce the discrepancy between the numerical and experimental results.

#### **4.3 Multi-physics simulation**

The patch antenna sensor measures structural strain by the shift in electromagnetic resonance frequency. To accurately describe both mechanical and electromagnetic behaviors of the antenna sensor, a multi-physics sequential coupled simulation approach is adopted. A 3D finite element model is built for both mechanical and electromagnetic simulations using the same geometry and meshing. In the mechanical simulation, nonlinear constitutive relationships of materials are considered for calculating accurate deformation under loading. Based on the deformed shape, the electromagnetic behavior of the antenna sensor is simulated. Partially air-filled cavity modelling technique is adopted for efficiently calculating the resonance frequency of the patch antenna sensor. The simulated strain sensitivity is compatible to that identified through laboratory experiment.

#### 4.4 Strain sensing performance

Compressive and tensile tests have been conducted to investigate the strain sensing performance of the designed patch antenna sensors. Laboratory tests validate that the patch antenna sensors are capable of estimating small strain on structures.

Compressive test is conducted to investigate the strain sensing performance of the RFID patch antenna sensor. The experimental results show that the strain sensitivity of the sensor is  $-874 \text{ Hz}/\mu\epsilon$ , and the corresponding coefficient of determination is 0.9945, which indicates strong linearity between resonance frequency change and strain.

The strain sensing performance of the RFID patch antenna sensor is validated through tensile test. The tensile test results show that the strain sensitivity of the RFID patch antenna sensor is  $-521 \text{ Hz}/\mu\epsilon$ , and the corresponding coefficient of determination is 0.9909, which confirms strong linearity between resonance frequency change and strain.

Tensile tests are conducted to investigate the strain sensing performance of the dual-mode RFID patch antenna sensor operating in both passive and active modes. The tensile test results show that the strain sensitivities of the sensor are  $-599 \text{ Hz}/\mu\epsilon$  and  $-582 \text{ Hz}/\mu\epsilon$  for passive and active modes, respectively. The coefficients of determination for these two modes are 0.9871 and 0.9787, which indicate acceptable linearity. In addition, using similar strength of wireless interrogation power, the active mode can achieve longer interrogation distance.

#### 4.5 Crack sensing performance

The crack sensing performance of the RFID patch antenna sensor has been investigated through the emulated crack test and the fatigue crack test. Test results have shown that the patch antenna sensor can detect surface crack in both tests.



In the emulated crack test, only deformation but no fracture occurs on the patch antenna sensor in the initial loading steps. The antenna resonance frequency slightly decreases as the deformation accumulates. When crack starts to propagate on the antenna sensor, a large drop of the resonance frequency can be detected. As the crack grows gradually through the antenna sensor, an approximately linear relationship between the crack width and the resonance frequency change can be observed from the test results.

In the fatigue crack test, resonance frequency of the patch antenna sensor keeps decreasing when crack propagates across the specimen. Approximately 1.5 MHz resonance frequency decrease is observed when the crack length increases to 0.8822 in. Compared with the emulated crack test, less linearity is observed in the fatigue testing data, which may result from the complicated deformation of the sensor during fatigue testing.

## 5 CONCLUSION

In this project, thermally-stable patch antenna sensors have been designed and validated for monitoring strain and crack growth of bridge structures. Extensive numerical simulation and laboratory experiments lead to the following conclusions.

The temperature-induced dielectric constant change can result in unwanted resonance frequency change in patch antenna sensors. The thermally stable substrate material is capable of improving the strain/crack sensing performance of patch antenna sensors by preserving the dielectric constant at different temperature levels.

Accurate simulation for the behaviors of patch antenna sensors depends on reliable material properties implemented in the FE model. Laboratory experiments have been conducted to qualify and quantify both the mechanical and electromagnetic properties of the substrate material. A model updating framework through numerical optimization can effectively reduce the discrepancy between numerical solution and experimental measurement. The updated material parameters help model predictions to match experimental results closely.

The developed patch antenna sensors are capable of measuring small structural strain. The structural strain can induce the change of electrical current length, and thus result in antenna resonance frequency shift, from which the strain can be wirelessly estimated. The strain sensing performance of patch antenna sensors has been validated through both the tensile and compressive tests. The experimental results demonstrate that an approximately linear relationship between the resonance frequency of the antenna sensor and the strain experienced by the sensor as the strain is insignificant. In addition, working in active mode, the dual-mode RFID patch antenna sensor can easily achieve longer interrogation distance with the assistance of external power source.

Although the dual-mode RFID patch antenna sensor requires cell battery for operating in active mode, the power management system is capable of harvesting the solar energy and recharging the cell battery. In this way, the sensor does not require periodic battery replacement. Even in the worst scenario in which the battery is depleted, this dual-mode RFID patch antenna sensor can work in passive mode and still provide wireless strain sensing.

Two scenarios of crack sensing performance are presented, including emulated crack sensing and fatigue crack sensing. The experimental results show that the RFID patch antenna sensor is capable of measuring small cracks and tracking crack propagation. As surface crack propagates, the resonance frequency of the antenna sensor decreases as expected. Measuring fatigue cracks induced by cyclic load still remains a challenge for patch antenna sensors. Weaker linearity between the resonance frequency and the fatigue crack length is observed during the test.

## 6 RECOMMENDATIONS DEVELOPED AS A RESULT OF THE PROJECT

Building on current research, recommendations on applying patch antenna sensors on strain/crack sensing are listed as follows:

- The temperature effect on resonance frequency of patch antenna sensors should be taken into consideration in measurements. Using thermally-stable substrate material can greatly reduce the resonance frequency change due to dielectric constant variation. However, this thermal effect cannot be perfectly eliminated. Calibration according to environmental temperature can lead to more accurate measurement results.
- Sensing consistency, particularly between compressive and tensile testing scenarios, needs further study. Detailed modelling and extensive experiments should prove helpful for investigating the difference between strain sensitivity of the antenna sensor in compressive and tensile tests.

In summary, harnessing the latest wireless and energy harvesting technologies, the research team has developed RFID-based patch antenna sensors demonstrated with potential in strain and crack sensing. Fabricated on thermally stable substrate, the antenna sensors operate at more steady resonance frequencies under temperature fluctuation. Equipped with a power management system, a dual-mode patch antenna sensor can achieve long interrogation distance in active mode, while maintaining the capability of strain sensing in passive mode when external power supply is not available. The designed patch antenna sensors enable a low-cost solution for large scale health monitoring of engineering structures.

## 7 REFERENCES

- [1] Yi, X., T. Wu, Y. Wang, R. T. Leon, M. M. Tentzeris, and G. Lantz, *Passive wireless smart-skin sensor using RFID-based folded patch antennas*. International Journal of Smart and Nano Materials, 2011. **2**(1): p. 22-38.
- [2] Yi, X., C. Cho, J. Cooper, Y. Wang, M. M. Tentzeris, and R. T. Leon, *Passive wireless antenna sensor for strain and crack sensing-electromagnetic modeling, simulation, and testing*. Smart Materials and Structures, 2013. **22**(8): p. 085009.
- [3] Yi, X., R. Vyas, C. Cho, C.-H. Fang, J. Cooper, Y. Wang, R. T. Leon, and M. M. Tentzeris, *Thermal effects on a passive wireless antenna sensor for strain and crack sensing*, in *Proceedings of SPIE, Sensors and Smart Structures Technologies for Civil, Mechanical and Aerospace Systems*. 2012: San Diego, CA, USA. p. 83450F
- [4] ASTM, *Standard Test Method for Tensile Properties of Plastics*. 2005, American Society of Testing and Materials.
- [5] Bruneau, M., C.-M. Uang, and A. Whittaker, *Ductile design of steel structures*. Vol. 389. 1998: McGraw-Hill New York.
- [6] Menegotto, M. *Method of analysis for cyclically loaded RC plane frames including changes in geometry and non-elastic behavior of elements under combined normal force and bending*. in *Proceedings of IABSE symposium on resistance and ultimate deformability of structures acted on by well defined repeated loads*. 1973. Lisbon, Portugal.
- [7] Hansen, N., *The CMA evolution strategy: a comparing review*, in *Towards a new evolutionary computation*. 2006, Springer. p. 75-102.
- [8] ASTM, *Standard test Method for Relative Permittivity (Dielectric Constant) and Dissipation Factor of Polymer-Based Microwave Circuit Substrates*. 2010, American Society of Testing and Materials.
- [9] Peng, Y., Y. M. Shkel, and G. Kim, *Stress dielectric response in liquid polymers*. Journal of rheology, 2005. **49**: p. 297.